50th AIAA Aerospace Sciences Meeting including the New Horizons Forum and Aerospace Exposition
09 - 12 January 2012, Nashville, Tennessee
AIAA 2012-0194

Pre-Ionization Plasma in a FRC Test Article

Ryan A. Pahl[1] and Joshua L. Rovey[2]
Missouri University of Science and Technology, Rolla, MO 65409

Pulsed plasma systems, specifically field reversed configuration devices, show great potential for future space propulsion systems. The fundamental formation process of heavy-gas plasma necessary for propulsion application is not well understood. The following study is focused on characterizing the pre-ionization stage of a field reversed configuration test article. Specifically, flux loop and B-dot probe data are presented and used calculate the magnetic flux and magnetic field strengths within MPX. Finally, plasma images collected with a high speed camera are presented. Tests are conducted at 15 and 20 kV using both air and argon over a pressure range of 2 – 70 mTorr and at atmosphere. Discharges with no plasma present have a frequency of 464 kHz while a discharge that produces plasma resonates at approximately 490 kHz. Details of probe construction and calibration are also presented. A maximum magnetic field of 882 G is observed for a 20 kV discharge with fill pressure of 45 mTorr of air near the edge of the theta coil. A maximum magnetic flux of 2.17 mWb is observed for a 20 kV discharge with a fill pressure of eight mTorr. The largest amount of energy absorbed by the plasma is 30.3 J and occurs during a 20 kV discharge in air at 60 mTorr. Peak magnetic fields, magnetic flux, and formation times as functions of gas species, pressure, and voltage are also presented. Maximum energy absorption into plasma occurs at 65 mTorr of air at a discharge voltage of 20 kV.

Nomenclature

A	=	area of loop
a	=	RC integrator forgetting term
B	=	magnetic field
β	=	ratio of plasma particle pressure to external confining magnetic field pressure
f	=	frequency
I	=	current
l	=	length of theta coil
n,N	=	number of turns
n_e	=	number density of electrons
n_o	=	number density of neutral particles
P	=	pressure
r_c	=	theta coil radius
TTL	=	transistor-transistor logic
t	=	time
μ_0	=	permeability of free space
V	=	voltage
V_{pp}	=	peak-to-peak voltage
Φ_v	=	vacuum magnetic flux

[1]Graduate Student, Mechanical and Aerospace Engineering, rap4yd@mst.edu, Toomey Hall, 400 W. 13 th St., Rolla, MO 65409-0050, and AIAA Student Member
[2]Assistant Professor, Mechanical and Aerospace Engineering, roveyj@mst.edu, Toomey Hall, 400 W. 13 th St., Rolla, MO 65409-0050, and AIAA Senior Member

I. Introduction

Field reversed configurations (FRCs) offer an attractive method of propelling future spacecraft. FRCs are a subset of the more general plasmoids known as compact toroids (CTs). CTs include both spheromaks, which have both toroidal and poloidal components of magnetic field ($B_z \approx B_\theta$), and FRCs, which only consist of poloidal fields ($B_z >> B_\theta$).[1] CTs are typically formed using pulsed inductive systems with large currents on the order of tens of kilo-amperes pulsed. The current is pulsed through strategically arranged inductive coils to induce a magnetic field and opposing plasma currents. Ultimately a magnetically self-contained plasma is desired. Internal currents of the plasma form a magnetic field separate from the applied field generated by the experiment allowing the detached CT (or plasmoid) to be accelerated and expelled to generate thrust.

FRCs have shown promise in recent years due to their ability to avoid the problems that plague typical electric propulsion systems. FRC formation is achieved through inductive means and expelled via a *JxB* Lorentz force. Because no electrodes contact the plasma during the formation process, FRCs have minimal boundary interaction with the plasmoid forming device. The lack of wall interactions prevents electrode erosion, a major factor in electric thruster lifespan. Using electromagnetic means to accelerate the plasma, FRCs can avoid the space-charge limitation encountered with gridded ion thrusters. With minimal wall interactions and no electrodes, FRCs avoid the technical challenges that plague other electric propulsion systems.[2]

Another attractive quality of FRCs is their potential for providing future spacecraft with a high thrust, high specific impulse propulsion system. With their emergence in 1958,[3] FRCs were initially investigated as an attractive fusion experiment due to their relatively high value of β (≈1 at equilibrium),[4] where β is defined as the ratio of plasma particle pressure to external magnetic field pressure and these early systems were able to achieve plasmoid translation velocities of 170 km/s in deuterium.[5]

FRCs for space propulsion application have been previously investigated at the University of Washington, University of Alabama-Huntsville, and at the Air Force Research Laboratory (AFRL) at Edwards Air Force Base.[6-13] These studies have mainly focused on lower energy FRC formation and translation with higher atomic mass gases.

Research performed at the University of Washington has investigated the use of FRCs for space propulsion and fusion, both individually and as a combined spacecraft system. Slough, *et.al.*, have investigated the Propagating Magnetic Wave Plasma Accelerator (PMWAC) device for space propulsion[6, 7] and also an earth-to-orbit fusion plasmoid device.[8] Both of these have similar operating principles. First, a FRC is created. Then the FRC is accelerated using a magnetic wave created by a sequence of pulsed electromagnetic coils. If the device is only providing propulsion, then the accelerated FRC is expelled at high velocity. However, if fusion is desired, then the FRC is compressed to smaller diameter causing the temperature to increase to fusion levels. Power can then be extracted for use creating the next FRC and the process is repeated. Results showed an ejection velocity of at least 1.8×10^5 m/s for each deuterium plasmoid, which yielded a total impulse bit of 0.3 N-s.[6]

The University of Washington in collaboration with MSNW LLC is also developing the Electrodeless Lorentz Force (ELF) thruster. The goal of the ELF device is to demonstrate efficient acceleration of a variety of propellants to high velocities (10-40 km/s) and operation at high power (e.g. >100 kW). The device is designed around a conical geometry with a rotating magnetic field current drive to ionize the gas and drive an azimuthal current to form an FRC.[14] Recent results show successful translation of a neon FRC with specific impulses up to 4,000 s and lifetimes on the order of 100 μs. Additionally, zero erosion or wall effects are present after 3,000 discharges.[15]

Investigations at the University of Alabama-Huntsville and NASA Marshall Space Flight Center have centered on the Plasmoid Thruster Experiment (PTX).[12, 13, 16, 17] PTX produces plasmoids using a conical geometry is used instead of cylindrical. This geometry has benefits because the FRC creation and acceleration occur within the same step. Unlike the PMWAC developed by Slough, a traveling magnetic wave is not required to accelerate the FRC. Results have shown electron temperature and density of 7.6 eV, and 5.0×10^{13} cm^{-3} for argon and 23 eV and 1.2×10^{14} cm^{-3} for hydrogen.[12] Exit velocities up to 2.0×10^4 m/s have been measured.

The electric propulsion group at Edwards Air Force Base constructed an annular FRC device called XOCOT.[9] The XOCOT project primary goal was to develop FRC-based plasmas at low power with long lifetime for propulsion applications. The program investigated different charging energies, voltages, and timing, as well as multiple propellants and pre-ionization techniques. Results showed multiple plasma formation and implosions are possible with densities and electron temperature on the order of 3.0x1013 cm-3 and 8 eV, respectively.[11] Current Air Force efforts in collaboration with Michigan Technological University are focused on understanding and quantifying the acceleration mechanism, plume profile, and plume energy of an FRC thruster.[17] XOCOT-T, the most recent version of the XOCOT experiment, is focused on the translation of FRCs formed at low voltages (0.5-3.0 kV) on longer time scales. This is accomplished with the use a three-turn conical outer coil and a pulsed gas puff valve. Several pressures and gas puff lengths have been investigated to determine optimal formation conditions.[5]

The fundamental goal of the Missouri Plasmoid Experiment (MPX) is to study the plasma formation process and elucidate the fundamental mechanisms that limit heavy-gases FRC formation efficiency. By studying the formation process, the loss mechanisms and energy profiles can be determined and incorporated into models allowing for better prediction of FRC characteristics. Presented studies are focused on measuring magnetic flux and magnetic fields generated by MPX using an array of flux loops and B-dot probes. The following sections first detail the experimental setup. Results from both internal and external probes are presented. Next, an analysis and discussion on the results is presented. Finally, the major conclusions of the paper are presented.

II. Experimental Setup

In order to analyze the formation characteristics of FRCs, a experimental test article needed to be constructed. This section will first focus on the fundamentals of the formation process. A detailed description of the test article, MPX, is presented. An brief summary of the pre-ionization stage is given. Finally, detailed information on probe design and construction is presented.

A. Design Considerations

While the pre-ionization of the plasma can be easily achieved, it has been shown that the FRC properties (stability, successful formation, end-state plasma properties) depend greatly on the specifics of the pre-ionization stage. This critical step is often overlooked, resulting in sporadic and inconsistent FRC formation.[18] The two most widely used techniques for pre-ionization are the axial and azimuthal pinch designs (Z-PI and θ-PI respectfully) due to their relative simplicity.[18] MPX uses a ringing theta pinch pre-ionization stage. First, the containment vessel is evacuated to a very low pressure and back filled with a neutral gas to a desired pressure. Previous FRC experiments have used a wide range of pressures (2-230 mTorr);[4, 9, 11, 18, 19] however, previous results have shown that lower pressures typically produce longer lasting FRCs at a cost of lower plasma temperatures.[18] After the containment vessel is filled, seed electrons are injected into the system and a bias magnetic field is applied using a low frequency discharge. The purpose of this stage is to trap a significant amount of magnetic flux withing the plasma allowing for increased plasmoid lifetime. While the bias field is applied, a second capacitor bank is discharged. This bank is what is typically known as the pre-ionization (PI) bank. This discharge tends to be at higher frequencies than the bias and main discharges. The higher frequency allows for increased plasma formation at lower energies[20]. The current produced by the PI bank flows through the theta coil generating an axial (poloidal) magnetic field. This field spins up an azimuthal current within the plasma. A final capacitor bank is then discharge through the coil in the opposite direction of the PI current. This sudden reversal of current is resisted by the plasma which has an internal field as a result of the PI discharge. As a result, the applied magnetic field lines "tear" away from the plasma and reconnect at the ends of the device (where the applied field is strongest due to current pooling) and results in a self-contained plasmoid (FRC). The applied field then compresses the plasmoid increasing its temperature. Finally, the internal plasma pressures increase to a point where they are equal to the applied field strength and equilibrium is reached (β≈1). Propulsion applications seek to expel this equilibrium plasmoid to generate thrust. The FRC formation process is also illustrated in Fig. 1.

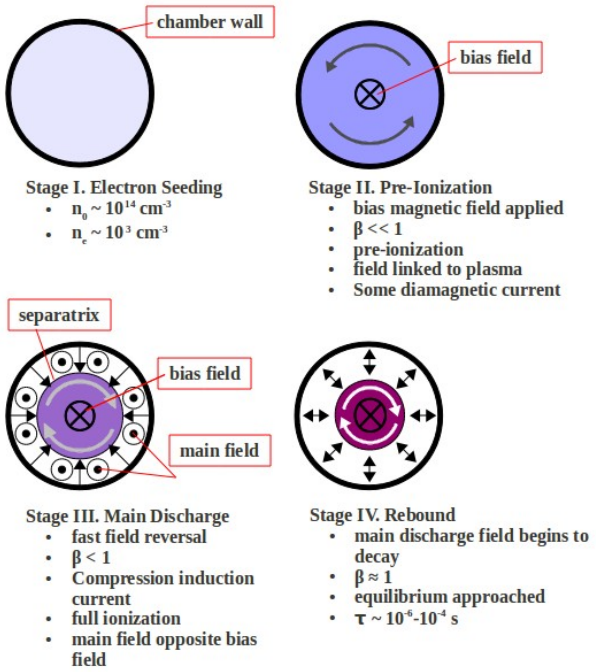

Figure 1: FRC Formation Process using a Field Reversed Theta Pinch Coil

B. MPX FRC Test Article

The MPX FRC test article is a quartz tube surrounded by a cylindrical copper theta pinch shell. Properties of the tube and theta pinch shell are given in Table 1. A grade 214 quartz with an inner diameter of 154.5 mm, outer diameter of 160.7 mm, and a length of 915 mm is surrounded by a copper theta coil with inner diameter of 178 mm, length of 762 mm, and thickness of 1.5 mm. The coil is formed with 12.7 cm long tabs that span the length of the coil. These tabs allow for easier connection to the other circuit components. To ensure that the quartz tube is centered radially within the theta coil, 9.5 mm thick acrylic spacers are machined and inserted between the coil and the quartz at both ends of the test article. The quartz tube is connected to the vacuum facility in the Aerospace Plasma Lab at Missouri S&T. Relative to the quartz tube, the coil is mounted with a spacing of 8.3 cm from the vacuum chamber and 2.5 cm from the end cap flange. The end cap is machined from aluminum and attaches to the quartz tube using a L-gasket. The theta coil has a L/D ratio of 4.29. The quartz tube is connected to the vacuum facility in the Aerospace Plasma Lab at Missouri S&T. Relative to the quartz tube, the coil is mounted with a spacing of 8.3 cm from the vacuum chamber and 2.5 cm from the end cap flange. The end cap is machined from aluminum. The gas feed through is located at the center of the aluminum flange to provide argon and xenon. The pressure within the quartz tube is measured using a Lesker KJL 6000 thermocouple gauge attached to the aluminum flange. L-gaskets are used to attach the quartz tube to the aluminum flange and the vacuum facility. A photograph of the test article is shown in Figure 2.

Table 1: MPX FRC Test Article Properties

Property	Quartz Tube	Theta Coil
Material	214 Quartz	Copper
Number of Turns	N/A	1
Inner Diameter [mm (in)]	155 (6.1)	178 (7.0)
Outer Diameter [mm (in)]	161 (6.3)	181 (7.1)
Thickness [mm (in)]	3.06 (0.12)	1.50 (0.06)
Length [mm (in)]	915 (36.0)	762 (30.0)
Inductance [nH]	N/A	37.2

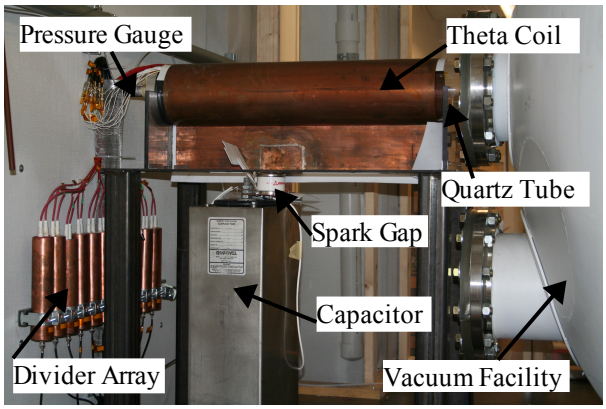

C. Pre-Ionization Discharge Circuit

The pre-ionization capacitor bank is designed to fully ionize the gas within the volume of the quartz tube contained within the theta coil. Assuming an ion production cost of 120 eV/ion, to achieve 100% ionization of argon, a total energy of 1.11×10^{21} eV (178.1 J) must be deposited into the given volume of gas assuming a fill pressure of 20 mTorr. Ceramic capacitors offer the best high frequency characteristics and Q factors and therefore were the primary consideration for MPX. However, no off-the-self ceramic capacitors were found capable of providing these high energy levels. As a result, an oil-filled capacitor is used for pre-ionization and its specifications are shown in Table 2. The maximum charging voltage of the pre-ionization stage of MPX is 30 kV, yielding a stored energy of 318.2 J. This is 179% of the energy needed to fully ionize the propellant assuming 120 eV/ion.

Table 2: Pre-Ionization Capacitor Specifications

Manufacturer	Maxwell
Voltage (kV)	70
Capacitance (uF)	0.707
Inductance (nH)	50

A simplified schematic of the pre-ionization circuit is shown in Fig. 3. The primary components of the pre-ionization circuit are the theta coil, capacitor, and spark gap switch. The capacitor is charged to an initial voltage level (15 and 20 kV in this paper) by a Matsusada RB30-30 power supply. A voltage divider network (see D.1.) is used to monitor the charge on the capacitor during both the charge and discharge stages. When the capacitor has reached the desired voltage, a Ross Engineering E40-2PNO high voltage switch is used to disconnect the power supply from the capacitor. An important note is that the connection is not only broken on the high voltage lead, but also on the ground lead. This isolates the capacitor from the charging system to prevent damage from high voltage and to ensure that the charging circuitry does not affect the discharge characteristics of MPX. After the charging

system is disconnected, a PerkinElmer TR-1700 transformer steps-up a low voltage AC signal to 28 kV, triggering the GP-14B spark gap switch to close. The GP-14B is a high voltage, high current three-electrode switch produced by PerkinElmer. The trigger (T) and adjacent (A1, A2) electrodes are placed close together while the opposite (O) electrode is placed farther away. The positive side of the capacitor is connected to the adjacent electrode and the low voltage side to the opposite electrode. The high voltage signal from the transformer is applied between the trigger and adjacent electrodes, ionizing the gas within the device. The presence of the plasma allows the opposite and adjacent circuits to conduct, discharging the pre-ionization capacitor. A Pearson 4418 current monitor (see D.1.) is placed around the negative terminal of the capacitor and records the current waveform of the discharge.

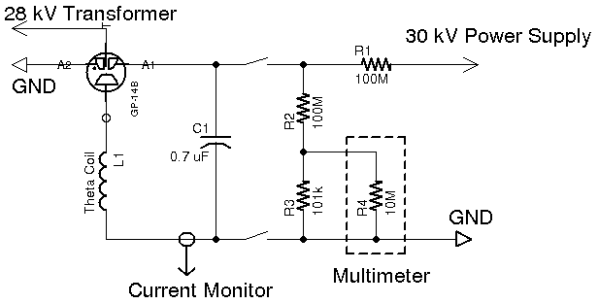

Figure 3: MPX Pre-Ionization Circuit Diagram

D. Probes and Data Acquisition

This section details the various external probes used to interrogate the plasma.

1 *Pre-Ionization Discharge Circuit*

The pre-ionization charge voltage and discharge circuit current are measured. Voltage is measured with a Fluke 78 multimeter. A voltage divider network consisting of a high voltage 100 MΩ, 10 W resistor and 101 kΩ 1 W resistor in series. The Fluke 78 multimeter is connected across the 101 kΩ resistor to measure the voltage. The multimeter has a 10 MΩ impedance and in parallel with the 101 kΩ resistor yields a resistance of approximately 100 kΩ. The ratio of the 100 MΩ resistor to the 100 kΩ resistor yields a voltage step-down of 1:1000. Current is measured with a Pearson 4418 current monitor (Fig. 4) with a peak current of 200 kA, maximum frequency of 2 MHz, and accuracy at 500 kHz of ±1 %. The current monitor is positioned around the negative terminal of the capacitor, which is connected to the capacitor body. An acrylic insert is pressure fit into the center of the current monitor. This ensures that the monitor remains centered about the capacitor terminal. A schematic showing the location of the probes is given in Figure 3.

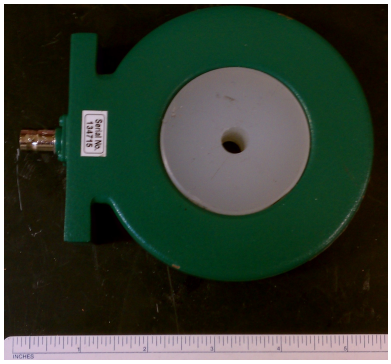
Figure 4: Pearson 4418 Current Monitor with Acrylic Insert

2 *B-dot probe array*

Magnetic probes are used to measure the time derivative of the magnetic field produced by the pulsed theta coil. A magnetic probe is basically a coil of wire. The physics of operation of magnetic probes (more commonly known as B-dot probes) is similar to a Rogowski coil and relies on Faraday's law. When the coil is placed within a time-varying magnetic field, a voltage is induced around the coil proportional to the number of turns, n, and cross-sectional area, A, through which the magnetic field is changing. This is expressed as Eqn. 1. Provided the "nA" constant for the probe is known, when the output of the probe is directly connected to an oscilloscope, the raw signal provides the time rate of change of the magnetic field. Integration of the raw signal then provides the magnetic field as a function of time, *B(t)*.

$$V_{probe} = n A \frac{dB_{coil}}{dt} \tag{1}$$

Coilcraft 1008HT-R56TGLB surface mount inductors are used for all B-dot probes. The surface mount inductors were chosen due to their well characterized frequency response and a small size. The 1008HT inductor has a 2.41 mm x 1.14 mm cross-section with a depth of 2.67 mm. The R56TGLB variant has an inductance of approximately 600 nH for discharge frequencies of 2 MHz or less. The nA constant of the R56TGLB inductor is 104.5 mm^2. The properties of the 1008HT surface mount inductor are provided in Table 3 and a picture is provided in Figure 5.

The B-dot probe array consists of ten Coilcraft 1008HT-R56TGLB surface mount inductors. The inductors are placed on the quartz tube such that the axis of the coil windings is parallel to the theta coil to measure the axial magnetic field and secured with tape. The first inductor is placed 2.5 cm inward from the side of the theta coil closes

to the vacuum facility. The remaining probes are spaced eight centimeters apart so that the tenth inductor also lies 2.5 cm from the opposite end of the theta coil. The probe locations are numbered sequentially one through ten with the tenth probe being the closest to the vacuum chamber. The probes are soldered to a short section of SMA coaxial cable. The SMA cable is then run along the wall of the quartz tube, away from the vacuum facility, and transitioned to RG223/U coaxial cable via a SMA to BNC adapter. The length of SMA cable used varies by location of the probe with probe one having the shortest length and probe ten having the longest. Because RG223/U cable is double shielded, it better insulates the data transmission cables from electrical noise generated during MPX discharges. This is the reason varied lengths of SMA are used even though identical lengths would provide more identical electrical properties. Only a small section of SMA is desired after the cable emerges from under the theta pinch coil before transitioning to RG223/U. The small variation in electrical properties that may be present due to varied cable length is deemed acceptable to achieve a cleaner signal. All RG223/U transmission cables are 5.33 m in length. The transmission cables run through a metal mesh along the wall of the building and under the metal platform that MPX is built upon. After the cables emerge below the platform, they are run through an aluminum electrical conduit. This seemingly superfluous cabling scheme provides increased shielding from the electromagnetic noise generated during an MPX discharge and provide cleaner, higher quality data. The RG223/U cable then connects to a Bird 20 dB 50 Ω in-line attenuator before connecting to the data acquisition system.

Table 3: Coilcraft 1008HT-R56 surface mount inductor electrical properties

Manufacturer	Coilcraft
Model Number	1008HT-R56TGLB
Inductance [nH]	600 @ 0.5 MHz 560 @ 25 MHz
Q Factor	2 @ 0.5 MHz 32 @ 100 MHz
Impedance [Ω]	4 @ 0.5 MHz
Self-Resonant Frequency [MHz]	485
DC Resistance [Ω]	1.9
I_{rms} [mA] (Max)	240
nA [turns-mm^2]	104.5

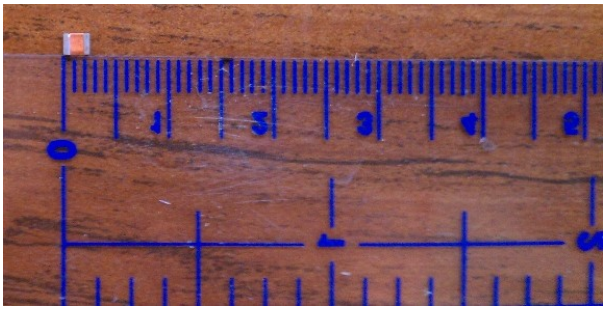

Figure 5: Coilcraft 1008HT-R56 surface mount inductor used for B_dot probes

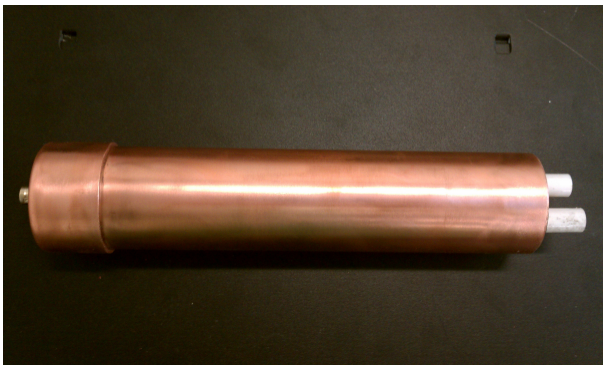

Figure 6: Finished voltage divider for high voltage output from flux loops

3 Flux loop array

Flux loops are used to measure the magnetic flux through the theta coil at a particular axial location. A flux loop is simply a single turn loop of wire between the quartz tube and theta coil. Due to the large magnetic flux generated by ringing theta pinch coils, a large voltage (kV) is induced within the flux loop. The flux loops used in MPX are made from a Wiremax SK 3020A high voltage wire. This wire is rated at 30 kVDC with an outer diameter of only 2.79 mm and fits between the quartz tube and theta coil. The high voltage signal is then stepped down using a custom built voltage divider network so that it can be processed by the data acquisition equipment. The custom voltage dividers provide a theoretical 154:1 step down when using a 1 MΩ terminated data acquisition system. A summarized construction method of the voltage dividers is included in this section. Complete details of the construction of the custom voltage divider can be found in the masters thesis by Um.[21] The voltage dividers constructed for this experiment are made from 25.4 cm segments of 5.08 cm diameter type M copper pipe. Alden high voltage connectors are used to connect the flux loops leads to the voltage divider. The high voltage leads attached to a custom made fiberglass end cap and uses a 0.32 cm diameter o-ring to provide a liquid-tight seal. Inside the copper pipe, the high voltage connectors are each attached to a string of 18 resistors in series, each measuring 56 Ω. The resistors are mounted to a small fiberglass board that resides withing the copper pipe measuring 5 cm x 25 cm x 0.48 cm. A 13 Ω resistor then connects the strings of 18 resistors.

A BNC connector is then placed in parallel with the 13 Ω resistor to provide the low-voltage output signal. A copper cap fits over the BNC connection and is glued in place. The electronics are protected from stray electrical discharges by dipping them in Super Corona Dope and baked. Each dip provides a two mil (0.001") thick coating with a rating of dielectric rating 4,100 V/mil (3,000 V/mil if not baked). The dip and baking cycle is completed three times to provide electrical protection of approximately 24 kV. A picture of the finalized voltage divider can be found in Figure 6. The output from the divider is connected to a 5.33 m RG223/U transmission cable and follow the same layout as the transmission cables used on the B-dot array.

The flux loop array is built in a similar manner as the B-dot probe array. Ten loops of Wiremax 3020A wire are wrapped around the quartz tube at the same locations as the B-dot probes and secured with kapton tape as shown in Fig. 7. As with the B-dot probes, probes one and ten are mounted 2.5 cm inward from the edge of the theta coil. The spacing between coils is eight centimeters. The probe spacing in MPX is slightly tighter spacing than the 8.25 cm used in FRX-L[22] and should provide sufficient resolution on plasma properties.

Figure 7: Array of ten flux loops wrapped azimuthally around quartz containment vessel prior to insertion into theta coil

4 High Speed Camera

A FASTCAM-1024PCI model 100k high speed camera provides a visual of the plasma formation. A frame rate of 109,500 fps with a shutter speed of 1/109,500 s is used to acquire the time evolution of the plasma. This gives an image at an interval of 9.1 μs. Using these settings, the high frame rate results in an image resolution of 128 x 16 pixels. The camera is mounted on the opposite side of the vacuum chamber where an acrylic flange allows internal viewing of the chamber. The camera interfaces with a dedicated 64-bit Windows 7 Enterprise workstation with an 2.66 GHz Intel Core 2 Quad (Q9400) processor and 8 GB of RAM.

5 Data Acquisition

Data are acquired using three 4-channel Tektronix DPO 2024 200 MHz 1 GS/s oscilloscopes. All three scopes trigger on the current monitor signal. The trigger in this experiment is set to -600 V with a decreasing slope. The 1:1000 signal attenuation of the current monitor results in an oscilloscope triggering voltage of -0.6 V. The horizontal divisions are set to four μs/div with the trigger set to -16.04 μs. Identical configuration of oscilloscopes ensures that all waveforms start at the same time ($t=0$). Vertical divisions vary by probe type. All channels measuring flux loop data are set to the save vertical divisions. The channels measuring B-dot signals are similarly set to a uniform value but not necessarily the same value used by the flux loops.

Output data from each oscilloscope are saved to separate USB drive using identical naming structures. This insures that test output data from different tests do not get combined and processed in an incorrect order. Each USB drive uses an uniquely named folder for identification (i.e., scope 1, scope 2, etc.). When a data set is recorded, each each oscilloscope writes the data to their respective USB drive in the uniquely named folder. The name used for this data set, however, is the same for all scopes.

Figure 8. Aerospace Plasma Laboratory Vacuum Chamber Facility

E. Vacuum Facility

The vacuum facility is 6-ft-diameter, 10-ft-long and evacuated to rough vacuum by a Tokuda rotary vane pump connected to an Edwards blower. High-vacuum is achieved with four 35-inch-diameter Varian oil diffusion pumps with a combined pumping speed of 200,000 L/s on air. The MPX test article is attached to a 16-inch-diameter

port on the rear of the facility. A custom flange is machined with a 146 mm OD centered hole. A different size step is added to both sides of the flange. On the side facing the vacuum facility, a 168 mm OD step is machined approximately 6.4 mm deep. This allows for a machined disk to be inserted to decrease the rate at which gases leave MPX and go into the vacuum facility. Without this "plug", back fill pressures above a few mTorr where unobtainable. A second step is machined on the side of the flange facing MPX with an OD of approximately 165 mm OD and 6.4 mm deep. This allowed the quartz tube to be mated to the vacuum facility via a Viton L-gasket. A picture of the facility is shown in Figure 8.

III. Results

This section presents the data collected from the various external probes used to investigate the plasma discharge properties of MPX. Because of the relatively large number of probes compared to the number of data acquisition channels not all probe signals could be recorded for every test. To fully characterize the plasma, a two subsets of probe combinations are used to interrogate the plasma. For a given voltage and gas species combination, data from half of the flux loops and B-dot probes are recorded. The first subset of probes consists of flux loops and B-dot probes at locations one through five. The second subset consists of flux loops and B-dot probes at locations six through ten. Subsequently, each voltage and gas species combination must be tested twice, once for each subset, to fully map the discharge characteristics of MPX. This methodology presents certain challenges, namely varied discharge characteristics. The discrepancies between discharges is discussed at greater length later in this and subsequent sections. The initial results of the external probes are presented. Finally, plasma discharge images obtained with the high speed camera are presented.

A. Testing Matrix

Two gas species are used in this experiment: air and argon. Both gases where tested at 15 and 20 kV over a large pressure range. The pressures tested are 0-20 mTorr in two mTorr increments and 25-65 mTorr (70 for argon) in five mTorr increments. The last pressure of interest is atmospheric pressure with air. This results in testing at 22 separate pressures.

1 Testing Methodology

The first set of tests are done to establish baseline measurements of the system. First, atmospheric shots for all twenty (ten flux loops and ten B-dot probes) probes were conducted on air only. Next, the vacuum facility brings MPX down to its baseline pressure of 2.2×10^{-5} Torr and the zero mTorr data are recorded for all twenty probes. At this pressure, it is assumed that neither gas species is present and these data are used as the zero mTorr data for both gas species. After these baselines are established, a methodical testing procedure is used to acquire the remaining data in the testing matrix. In previous testing, the SMA 50 Ω terminator proved to be rather fragile. To protect the probes and connectors from unnecessary wear, the probe subsets were switched as infrequently as possible. For the first phase of testing, the first subset of probes (flux loops and B-dot probes one through five) are connected. The charging system is set to 15 kV and a 10 SCCM Alicat Scientific flow controller is used to slowly fill MPX to the desired fill pressure with air. Once the desired pressure is reached, MPX is discharged and the resulting data recorded. This process is repeated through the entire pressure range. After the last pressure is tested, the system is again returned to its base pressure. Argon is no connected to the flow controller and is used to slowly fill MPX to the same pressures as with air. After testing with argon is completed, approximately a quarter of the testing matrix is complete. The second subset of probes is now connected to the data acquisition system and the entire process repeated for argon and then air for all pressures, completing half of the desired testing matrix. This completely maps the MPX discharge properties at 15 kV. Next, the 20 kV test is conducted. The HV charging system is set for 20 kV and tests are conducted in the same fashion as the 15 kV tests. The difference, however, is that second probe subset is tested first to avoid wear on the connectors.

Unfortunately, an electrical short during the 20 kV testing resulting in damaged to the charging system. As a result, only a partial mapping is completed for the second probe subset. All pressures with air are complete, but argon is tested only to ten mTorr. No probe subset one data are available. However, the data that were collected still fully characterize the 15 kV discharge and the partial 20 kV discharge sheds light on trends seen when additional energy is added to the system. Because of this large testing matrix, a limited number of tests that are representative of observed trends are presented in the following sections.

B. B-dot Probes

A typical sample of data collected from probe one of the ten B-dot probe array are presented in Figure 9. Data shown are from a discharge at zero and eight mTorr to highlight effects of plasma formation on probe output. The zero mTorr (high vacuum ~10^{-5} Torr) case is shown in black with the eight mTorr case in red. It is evident from the data that plasma formation alters the waveform substantially. The frequency of the discharge without plasma is 462 kHz and there are eleven complete periods of oscillation. The eight mTorr discharge is good agreement until 3.29 µs. At this time, the red waveform diverges from the black indicating that something within the system is altered from the no plasma case. Unfortunately, the high speed camera does not have sufficient temporal resolution to determine the instant when plasma is visually generated. Therefore, while plasma is visually present during the discharge, it cannot be said that this deviation represents the time when the plasmoid physically forms. The frequency of this discharge changes substantially after the deviation point. The frequency post-deviation increased by 6% to 490 kHz and only ten full periods are completed. The B-dot probes indicate that in the presence of plasma, the time-varying magnetic values field decreases faster near the coil wall and increases in frequency compared to cases when plasma is not formed.

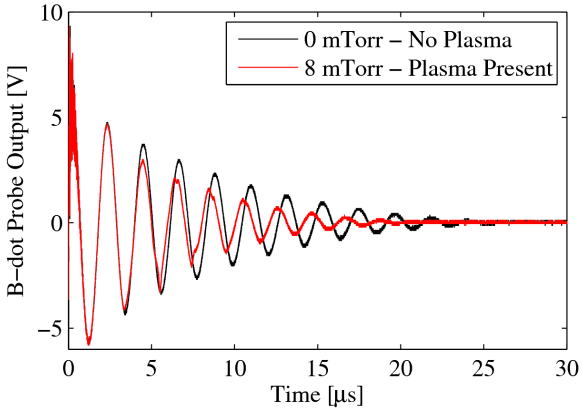

Figure 9: B-dot data from position one during a 15 kV discharge in zero and eight mTorr of air

Data from all ten B-dot probes during a 15 kV discharge in air at zero mTorr are presented in Figure 10. The figure shows only a small portion of the data so that differences between probe signals can be observed. No data processing is present. The most evident trend is that the various probe outputs are out of phase with each other. A possible phase shift could be due to the method of data acquisition. Since probes one through five represent one discharge and probes six through ten another, a slight difference in the timing between discharges could account for a small shift. However, if this is the case, the five probes in either test should be grouped together and two distinct phases would be seen. This is not the case. Probes four, five, seven, eight, and ten have the least phase shifting while the remaining probes have varied degrees of phase shifts. Probes one and nine are nearly 90º out-of-phase. Integration of a signal would produce a phase shift of 90º, however; the magnitude of the outputs does not show the attenuation typically seen with integrated signals. This trend is observed in all the data and is not limited to this one case. At different pressures, the phase-shift between from one probe relative to the others remains constant. This indicates that the probes are operating in a repeatable fashion, but the construction of the array or the physical layout of MPX is affecting the probes.

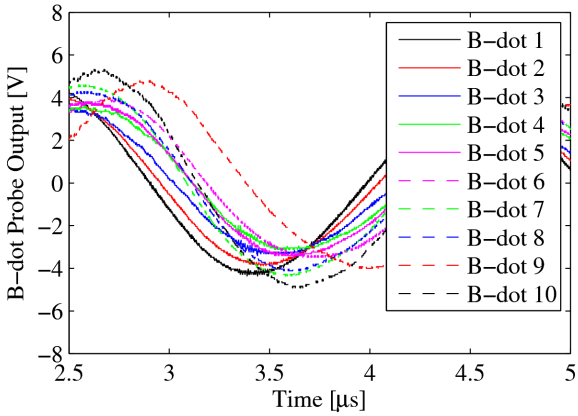

Figure 10: Output of B-dot probe array during a 15 kV discharge in zero mTorr of air

Also observed during this discharge is the variation in amplitudes of the waveforms. Probe ten consistently produced the largest signal. The percent difference from probe ten signal to that of the lowest amplitude signal, probe four, is 36.6%. When comparing the probe outputs to the average output of all ten probes, the smallest percent difference occurred is 1.4% at location two. Probe four shows the greatest deviation from average with a percent difference of 26.2%. While the magnetic field within the theta coil is not expected to be uniform, the expectation is that the data would be symmetric about the center of the theta coil. It is clear from Fig. 10 that this is not the case.

One possible explanation for the discrepancies observed in the B-dot probes is the amount of transmission line present near the probe location. As mentioned previously and shown in Fig. 7, the transmission cables for the B-dot probes and flux loops run axially along the length of the quartz tube. The presence of conductive material near the probes can alter the readings of the probes. Additionally, the cables can develop a capacitive coupling that can also affect the data recorded. This challenge will be addressed in future work.

C. Flux Loop Probes

Flux loop data from the same discharge in Fig. 9 is shown in Fig. 11. Nearly identical trends are observed. Both pressure traces agree for the first full period of oscillation. Deviation is noted at 3.3 µs in this plot. This is less than a one percent difference in the deviation time of the B-dot probes. The discharge frequency of the no plasma case is 464 kHz with eleven full oscillatory periods. The eight mTorr discharge frequency after deviation is 489 kHz and only eight periods are observed. The frequencies are similar to those recorded by the B-dot probe in both the no plasma and plasma present cases. The flux loops indicate that the presence or formation of plasma decreases the time-varying magnetic flux generated by the theta pinch coil.

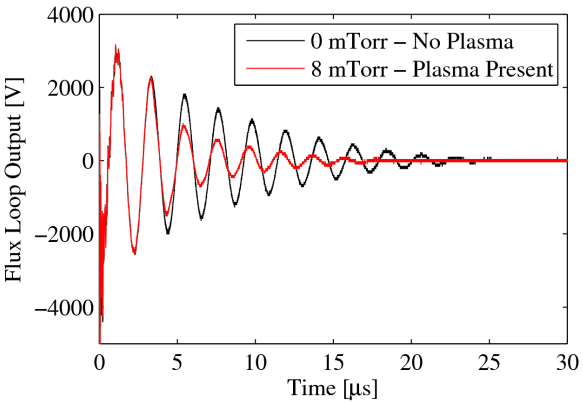

Figure 11: Flux loop data from position one during a 15 kV discharge in zero and eight mTorr of air

Data collected from all ten flux loops during a 15 kV discharge in air at zero mTorr are presented in Figure 12. As seen with the B-dot probes, the amplitude of the raw waveforms vary between probes. For comparison of values, the first peak after the discharge is analyzed at 1.15 µs. Flux loop five generates 3.60 kV, the largest signal of the ten probes. The smallest signal recorded is 3.11 kV by probe one. The percent difference between these values is 15.8%. The percent difference from the average peak output range from 5.6% to 9.3%.

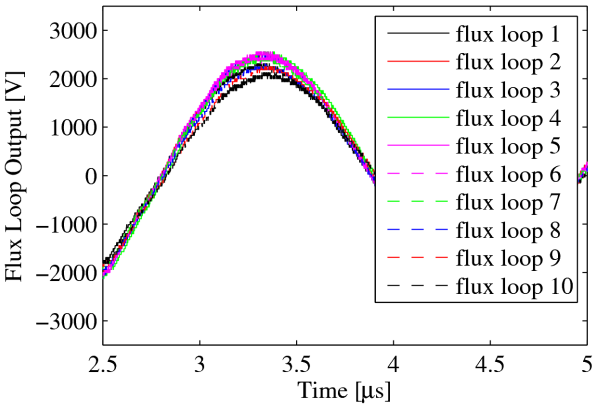

Figure 12: Output of B-dot probe array during a 15 kV discharge in zero mTorr of air

D. Plasma Discharge

High speed images of the plasma discharges are taken with the FASTCAM-1024PCI camera. The camera uses a 5 V TTL trigger. When the voltage is between 0.0 and 0.8 V, the TTL sees a "low" signal. At voltages 2.2 to 5.0 V, the TTL outputs a "high" signal. The oscilloscopes are set for a -0.6 V falling edge signal. This means that the two systems will trigger at different times. Because of the large range of triggering voltages (2.2 – 5.0 V), the camera can trigger at different points for a given discharge. Since, the output cannot be directly correlated with the MPX discharge data, these results provide merely a qualitative interpretation of MPX plasma formations. Furthermore, the TTL trigger distorts the output from the current monitor. This resulted in a separate test using the high speed camera that is independent of the large testing matrix described previously. However, due to the repeatability and reliability of the early times of MPX discharges before plasma is present, the plasma formed during these tests should be similar to those produced during previous mentioned testing. A small sample of plasma shots is presented in Figure 13. More plasma pictures are presented in section IV.G.

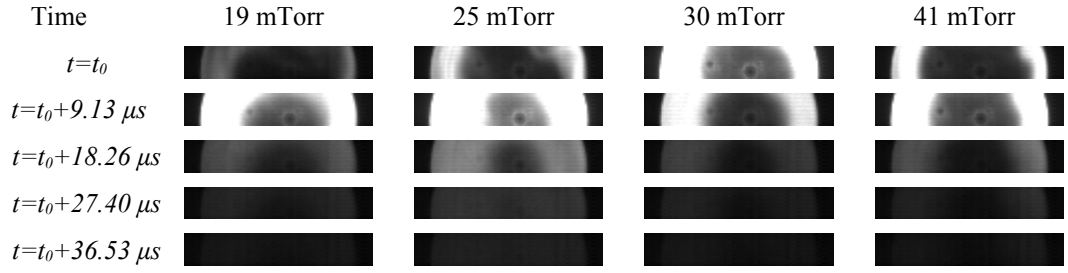

Figure 13: High speed images of plasma discharge take at pressures: 19, 25, 30, and 41 mTorr

IV. Analysis and Discussion

A. Calibration of Surface Mount Inductors

This section details the method of calibration used for the surface mount inductors used measure the time-derivative of magnetic field during MPX discharges. First, analytical calculations are applied. Calibration via Helmholtz coil is also investigated. Finally, results are compared to simulations.

1 Analytic Calculations

Analytical calculations using results of Faraday's law (Eqn. 1) is the first method of calibrating the magnetic probes. The data recorded by the probe *is* the time-derivative of magnetic field but scaled by some constant. This constant is known as the "nA" constant which is the product of the number of turns in the probe and the area of the probe. Coilcraft could not provide specific dimensions or number of turns due to the proprietary reasons. However, they did provide product of the area and number of turns for use in this research. Data recorded by the B-dot probes are integrated as shown in Eqn. 2.

$$\int_{t_i}^{t_f} V(t)\,dt = nA \int_{B_{t_i}}^{B_{t_f}} dB(t) = nA\left(B(t_f) - B(t_i)\right) = nA\,B(t_f) \tag{2}$$

At early times ($t < t_i$) MPX is charged, but no current is flowing so no magnetic field exists within the theta coil thus $B(t_i)$ is zero. By dividing both sides by nA, the magnetic field at any time after t_i can be found as shown in Eqn. 3.

$$B(t_f) = \frac{1}{nA}\int_{t_i}^{t_f} V(t)\,dt \tag{3}$$

2 Helmholtz Coil

Calibration using a Helmholtz coil is also used to calibrate the magnetic probes as a Helmholtz coil produces a purely axial magnetic field along its centerline. A custom built Helmholtz coil is used in the calibration of the magnetic probes. For more information on the construction of the Helmholtz coil see Ref. 23. For information on DC calibration of Helmholtz coils see Lucien[24] and Smith[25].

After DC calibration of the Helmholtz coil, an AC waveform can be applied to the coil to calibrate the magnetic field probes. The challenge encountered with this method is that a relatively large magnetic field is needed to generate an output from the surface mount inductors that can be accurately measured. A Rigol DG1022 function generator set at 5 V_{pp} is connected to a Crown CE2000 amplifier. The function generator is capable of generating a sine wave with a frequency up to 20 MHz. However, the Crown amplifier is only rated to a frequency of 20 kHz to maintain its listed power output of 1,950 W. Frequencies close to the discharge frequency of MPX where chose for testing. At 150 kHz, the output of the amplifier is 31 mV_{pp}. This corresponds to only a fraction of a Gauss (Ref [23]. Figure 8). The corresponding output from the B-dot probe is approximately 1.1 mV_{pp}, well within the noise of the oscilloscope. At higher frequencies, the current input into the Helmholtz coil decreases but the B-dot probe output remains the same indicating that the output is not sufficient to be viewed on the data acquisition system. As a result, this method is not being used to calibrate the B-dot probes.

3 Numerical Simulations

Computer simulations using a commercially available off-the-self software package, EMC Studio, is used to provide a check to the analytical calibration used above. The coil geometry is replicated within the software. To simulate the capacitor discharge, a sine wave with a frequency and amplitude of 450 kHz and 28 kA, respectfully, are set as the user defined source. The 28 kA comes from the discharge current associated with the 15 kV tests. An array of probes are placed within the simulated geometry and provide the magnetic field output. For more information on EMC simulations of MPX, see Ref. 23.

A sample of the probe outputs is shown in Fig. 14. Data from four probe locations are shown with the peaks indicated. The probes along the wall and the centerline in the center of the theta coil show identical field strengths. Additionally, both probes are farthest from the ends of the coil meaning they experience reduced end magnet field effects and approach an ideal solenoid. The lowest field strength is seen at the probe placed on the centerline 45 cm

from the center of the coil so that it resides approximately 7 cm outside of the theta coil. This minimum is expected as the field strength should degrade rapidly outside of the theta coil. The field strength at the center of the coil is found to be 460 G. The ideal solenoid equation (Eqn. 4) is used to verify the values at the center of the coil.

$$B = \frac{\mu_0 N I}{l} \tag{4}$$

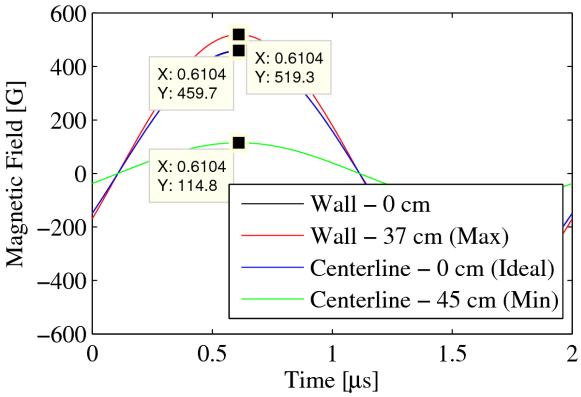

Figure 14: Output of an EMC Studio simulation of a 15 kV (28 kA) discharge

Results from EMC Studio with a current of 28 kA resulted in a field of 460 G along the at the center of the theta pinch coil compared to 462 G from ideal solenoid theory, an error of 0.5%. The highest magnetic field in the simulations is 519 G and is located 37 cm from the center (zero cm axially) of the theta coil. This is believed to be due to the pooling of current along the edge of the solenoid. With a higher current density in that region of the coil, a higher magnetic field would result. The is a 13% increase in field strength over the magnetic field at the center of the theta coil. The results from EMC Studio are similar for 38 kA. EMC predicts a field of 624 G at the center of the coil. Comparing to 627 G from ideal solenoid theory gives an error of 0.5%. The maximum field is found to be 703.9 G at 37 cm from the center along the wall of the coil. The minimum is again found at 45 cm on the centerline and is 156 G.

The values at the center of the coil are compared to the integrated data from B-dot probes at locations five and six as these are the closest to the center of the coil. For the 15 kV discharge, probes five and six record a maximum value of 4.78×10^{-6} V-s and 5.24×10^{-6} V-s, respectfully, at zero mTorr. Dividing the maximum values by the predicted field strength of 460 G yields the nA constants: 104.0 turns-mm^2 and 114.0 turns-mm^2 for probes five and six, respectfully. This an error of 0.5% and 9.1%, respectfully, when compared to the 104.5 turns-mm^2 provided by the manufacturer. At 20 kV, data exists for only the B-dot probe at location six. The maximum value recorded is 7.06×10^{-6} V-s. Dividing the 624 G predicted values by this maximum yields the nA constant of 113.1 turns-mm^2 and an error of 8.3% over the manufacturer nA and 0.7% from the 15 kV discharge. The nA constants from probe six are first averaged and the result averaged with the nA from probe five to obtain 108.8 turns-mm^2. This nA constant is used on all B-dot data to obtain the magnetic field at the various probe locations. The percent difference from probes five and six are 4.6% and 4.2%, respectfully.

The effective area of a magnetic field probe will change as a function of area since the probe is in essence an electrical choke that resists high frequency signals. However, for a given frequency, the nA constant should remain the same regardless of discharge voltage. The probes are designed with a self-resonating frequency of 485 MHz, several orders of magnitude greater than anything seen during a MPX discharge. The inductance of the probe provided by the manufacturer is 560 nH at 25 MHz. The manufacturer's website provides tools for determining the inductance at a given frequency. At 500 kHz, an inductance of 600 nH is found. The percent difference between these two values is 6.7%. However, this range encompasses a larger frequency spectrum than what is typically observed during a discharge. For a range more applicable to MPX (1 kHz – 1 MHz), the probe inductance is constant at 600.23 nH. The inductance at 25 MHz is actually the lowest inductance value that the probe will have over its entire operating range. At 100 MHz the inductance rises to 596 nH. The result is that over the frequency range of DC to 100 MHz, the maximum uncertainty in measurements due to probe electrical properties as a function of frequency should not exceed 6.7%. Combined with the error from probe calibration, an uncertainty of 11.3% is present in the magnetic field calculations.

B. Calibration of Flux Loops

This section outlines the calibration method of the high-voltage voltage dividers and the flux loops use in MPX.

1 High-Voltage Voltage Divider

One challenge faced when calibrating the voltage dividers is that function generators output an alternating waveform on the center conductor of a BNC cable while grounding the outer conductor to provide electromagnetic shielding for more accurate waveforms. By connecting the function generator to the voltage divider, one the resistor strings is grounded. Data acquisitions systems employ a similar technique to shield data being measured as well.

This means that when an oscilloscope is connected to measure the output and a function generator connected to provide input, one of the resistor strings is grounded. The current finds an easier path through building ground that through the 1008 Ω resistor network. A solution presented itself in the form of a Pearson 4100 current monitor. The flux loops are calibrated using a similar setup as the B-dot probes with one key difference. Instead of a Helmholtz coil, the output of the Crown amplifier is connected across a 1 Ω, 10 W resistor. The Pearson 4100 current monitor with an output of 1 V/A is used to monitor the current output of the amplifier. Since the resistor did not provide a large inductive load, more current is achieved in this configuration that in testing with the Helmholtz coil. When operated at 50 kHz, the amplifier output 4.0 A peak-to-peak which is then output as a 4.0 V_{pp} signal by the current monitor. At 500 kHz, the amplifier is capable of providing 316 mA_{pp}. The current monitor is capable of providing a true AC waveform since it is not grounded by the amplifier or function generator. The output of the current monitor is connected to the inputs of the voltage dividers and an oscilloscope is used to measure the output. The oscilloscope is set to record 128 sets of data and output the average peak-to-peak value. At 50 kHz, the output of the voltage divider is 25.81 mV. Comparing this to the input of 4.0 V, a ratio of 154.4 is calculated. A frequency sweep of the voltage divider from 50 kHz to 750 kHz yields an average attenuation of 153.89. The largest error is observed at 560 and 570 kHz and is 5.04% and 3.46%, respectively. The error in the measured attenuation and the numerically calculated attenuation is 0.06%. These values are deemed to be acceptable and an attenuation of 153.89 is used during post-processing.

2 Flux Loops

Calibration of the flux loops is achieved though Eqn. 5

$$\phi_v = B_v \pi r_c^2 \quad , \tag{5}$$

where Φ_v is the vacuum magnetic flux, B_v is the vacuum magnetic field, and r_c is the inner radius of the theta coil. This equation illustrates that the accuracy of the output of the flux loops is linearly dependent on the accuracy of the magnetic field probes. Any errors in calibration of the magnetic field probes will compound with other errors encountered by the flux loops.

Because the end effects of a finite solenoid diminish axial near its center, probes five and six will be used to calculate calibration values to avoid errors introduced by end effects. First, vacuum magnetic flux is calculated using the inner radius of the theta pinch coil and the magnetic field generated by a 15 kV (28 kA) discharge. Using the 460 G result from EMC Studio, the theoretical magnetic flux at the center of MPX is 1.14 mWb. The maximum integrated output values from probes five and six are 1.75 mV-s and 1.64 mV-s, respectfully, at zero mTorr. Dividing the predicted magnetic flux of 1.1 mWb by the peak values yields the calibration factors: 0.655 Wb/(V-s) and 0.697 Wb/(V-s) for probes five and six, respectfully. The percent difference in these calibration factors is 6.46%. The calibration factors are then averaged to get the final flux loop calibration value, 0.6758 Wb/(V-s). The error between the average value and the calibration factor of probes five and six are 3.13% and 3.23%, respectfully.

C. Post Processing

This section details the method of post processing used to generate magnetic field and magnetic flux data for analysis. Three methods of integration are briefly discussed. An example of the post-processing technique used in this paper is also presented and discussed.

1 Methods of Integration

Three methods of integration are possible to analyze data: passive RC integrator, active RC integrator, numerical integration. The first two methods utilize small electrical circuits to integrate the voltage. The benefit of the passive RC integrator is the simplest of the physical integrators to construct. A single resistor and capacitor are needed. The resistor and capacitor are connected in series. The signal is feed into the resistor and the capacitor connected to ground. The output is measured across the capacitor. The time constant of the circuit is defined as the product of the resistance and capacitance and must be large compared to the period of the waveform being integrated.[26] However, since a passive RC integrator is essentially a low-pass filter, the high frequency output signal is significantly attenuated (40 dB or more) making it difficult to accurately measure the output signal. An active integrator attempts to rectify this by actively amplifying the output of the RC integrator with an op-amp. This provides signals that are easier to measure with an oscilloscope but drifting of the DC offset can result in significant error over longer periods of time. The last method is to acquire the data without a physical integrator and use a computational software to numerically integrate the data. This method eliminates the attenuation issue caused by passive RC integrators and

the DC offset drift associated with op-amps. The main difficult is that unlike RC integrators that provide the desired output immediately, time consuming calculations are needed. The numerical integration option is the method chosen to analyze the data in this paper. The reduced error in probe measurements gained by eliminating hardware outweighs the increased time needed for data processing.

2 *Simulating an RC Integrator*

A challenge encountered with numerical integration of the data is that the resulting integral tends to drift away from zero. The reason for this is clear when considering the shape of an under-damped RLC discharge. The times before the discharge, no current is flowing in the system so waveform has an amplitude of zero. When the discharge occurs, the system quickly rises to its maximum peak. The waveform will then decrease to its lowest value. For a perfect sine wave, the amplitude of this "trough" is the same as the first peak. For an under-damped waveform, every is slowly dissipated and the amplitude of the trough is slight less than the previous peak. The amplitude of the next peak is then slightly less than the proceeding trough. This dampening continues until all energy in the system is dissipated and the waveform finally reaches steady state back at zero. However, when this signal is integrated, the area of the first peak is greater than the area of the first trough resulting in a net gain in total area. The is true of all the entire waveform. Integrating the waveform of any trough produces an area that will always be less than the area of the previous peak. As the areas are summed together, this net gain in area produces an offset and prevents the waveform from returning to zero. This is more clearly illustrated in Figure 15. After 25 μs, the probe stops producing a signal. This is because the current flowing through the theta coil has abated and no time-varying magnetic field is present. However, when looking at the integrated data using the trapezoidal rule, it appears that the magnetic field is still present and increasing linearly. As this is not physically the case, methods to account for this drift were investigate. The simplest solution to the problem would be to calculate the drift area increase as a function of time and subtract the drift from the integrated signal. Since a direct calculation of the drift is not possible, the most obvious approximation would be to assume a linear increase with time. Using the first and last points of the data series. With a known y-intercept of zero, an equation can be calculated using the point-slope method. This new waveform can then be subtracted from the original data set to obtain a corrected integral. This method works well for discharges where plasma is not present. However, the deviations like those observed in Figs. 9 and 11 result in a drift that the previous drift equation no longer models. Two models, one before and one after the discharge, were generated for these cases with mixed results. This required visually inspecting every data set to pinpoint the exact moment that the deviation occurs. Since this time varies from shot to shot, the time and effort required to utilize this method disqualified it as a means of accounting for the drift. Instead, however, an algorithm using the first order approximation of a RC integrator is used. Essentially, the model replicates the integration done by a physical passive RC integrator. The algorithm is the same as the trapezoidal rule with a "forgetting" term, *a*, added as shown in Eqn. 6.

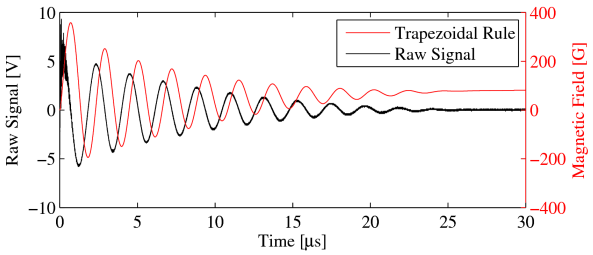

Figure 15: Raw B-dot signal and its calculated integral using the trapezoidal rule

$$B(t_2)=\frac{1}{nA}\frac{V(t_2)-V(t_1)}{2}dt+(1-a)B(t_1) \quad (6)$$

The term *(1-a)* tells the model to only remember a portion of the previously integrated signal. RC integrators "forget" data over time and the amount of data forgotten is a function of the RC time constant. By adjusting the correction factor, passive RC integrators with different RC time constants are modeled. The result of various correction terms on a the integration of a B-dot dataset is shown in Fig. 16. As the correction value approaches zero, the waveform goes to pure trapezoidal integration. By increasing the correction factor (previous information is forgotten faster), a smaller RC time constant is

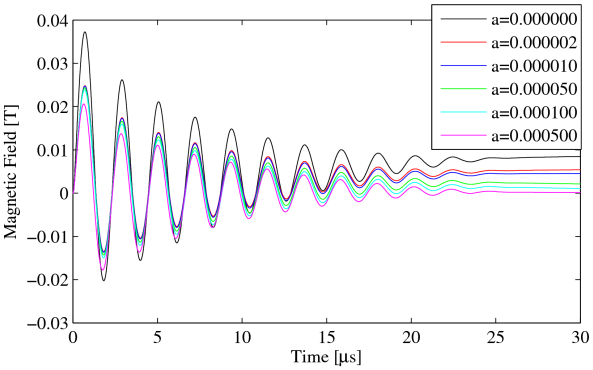

Figure 16: Comparison of "forgetting" correction terms on integration of B-dot probe data

simulated. As the time constant decreases, the resulting signal diverges from the actual integral. Since the trapezoidal rule represents the "pure" integral of the signal, and waveform that is in phase with the trapezoidal rule waveform is properly integrating the data. Figure 16 shows that as the correction term increases, the resulting waveform is significantly attenuated. Even a correction term as small as 2 x 10^{-6} is sufficient to cause an attenuation of 33.4%. This correction factor corresponds to a time constant of 231 μs which is larger than the 200 μs used to the value use in the physical RC integrators used in FRX-L.[27] Additionally, this small correction factor brings the tail of the waveform closer to the time axis as is demanded by the physical system. Further increasing of the correction factor results in more attenuation, but less than the decrease seen from $a=0$ to a=2 x 10^{-6}. The phase shift seen in the values a=1 x 10^{-4} to 2 x 10^{-6} are small. This means that the model is still accurately integrating the waveform but with slightly increasing attenuation. From Fig. 16, it appears that a correction factor of 5 x 10^{-4} would be sufficient. However, due to variations in datasets from the various probes, this factor is not sufficient to re-center the waveforms about zero. A value of 8 x 10^{-4} is found to be sufficient and is used during calculations of magnetic field and magnetic flux.

To account for the attenuation mentioned above, a few variations of the integral are considered. These are highlighted in Figs. 17 and 18. Both figures are of the same methodology, however, Figure 17 provides a zoomed-in view of Figure 18 to better show the effects of the post processing on the amplitude of the data. Figure 18 provides a full picture of the effects of the method employed and is more convenient for determining if the waveform is centered about zero and the relative phases. First, the raw data are plotted for comparison with the integrated data. The data obtained using both the trapezoidal rule and the simulated passive RC integrator are plotted. Due to error within the data acquisition system, a small amount of noise is present. Therefore, the value about which the simulated RC data are centered will be very close to zero, but may sit just above or below zero. The difference between the simulated RC integrator and trapezoidal rule are most evident in Figure 17. The amplitude of the simulated RC integrator is attenuated relative the the trapezoidal rule. To compensate for this, a series of data manipulations are used. First, the data from the trapezoidal rule are drift adjusted. This is done using the technique mentioned above. An average slope of the data is calculated and then subtracted from the trapezoidal rule data. This is done to attempt to re-center the trapezoidal rule data about zero for the early times. As a result, the first peak of the drift adjusted trapezoidal rule data will be close to the actual peak seen by the system. This is because the trapezoidal rule provides a "true" derivative of the signal with no attenuation. Next, the peak values of the drift adjusted trapezoidal rule data and simulated RC integrator data are found. The ratio of of these two quantities is then used to scale the simulated RC integrator data. The small offset error due to the data acquisition system is also amplified resulting in a rather large translation of the data along the y-axis. Since this value is constant, it can simply be subtracted from the scaled simulated RC data.

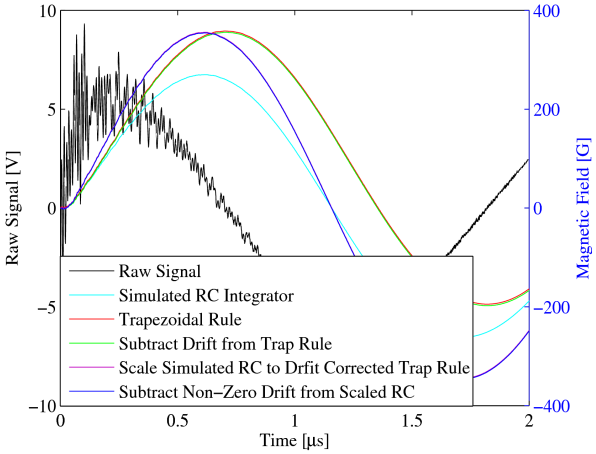

Figure 17: Methodology used to integrate probe data demonstrated on B-dot probe one data in air at 15 kV and zero mTorr and zoomed in on first peak of waveform

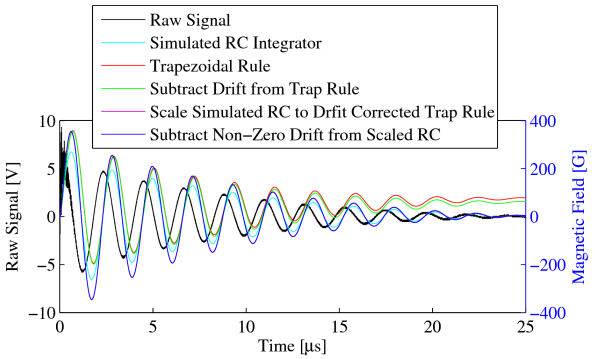

Figure 18: Methodology used to integrate probe data demonstrated on B-dot probe one data in air at 15 kV and zero mTorr

The result of this series of manipulations is a waveform that is still approximately 90° phase-shifted from the raw probe data and matches the peak value of the "true" integral. The method outlined in this section is used to integrate all B-dot and flux loop data.

D. External Measurements

This section compares probe readings as functions of time and location for different pressures. The trends observed in the data are then discussed. Data from only five distinct pressures are discussed for brevity.

1 B-dot

Data acquired on the B-dot probes is discussed in this section. Figure 19 is a contour plot of the magnetic field recorded by all ten B-dot probes for a 15 kV discharge as a function of probe location and time. Similarly, Figure 20 presents the same data but with argon as the fill gas. Figure 21 plots a 20 kV discharge in air. It is different from the other two figures as data from only five probes (probes six through ten) are available.

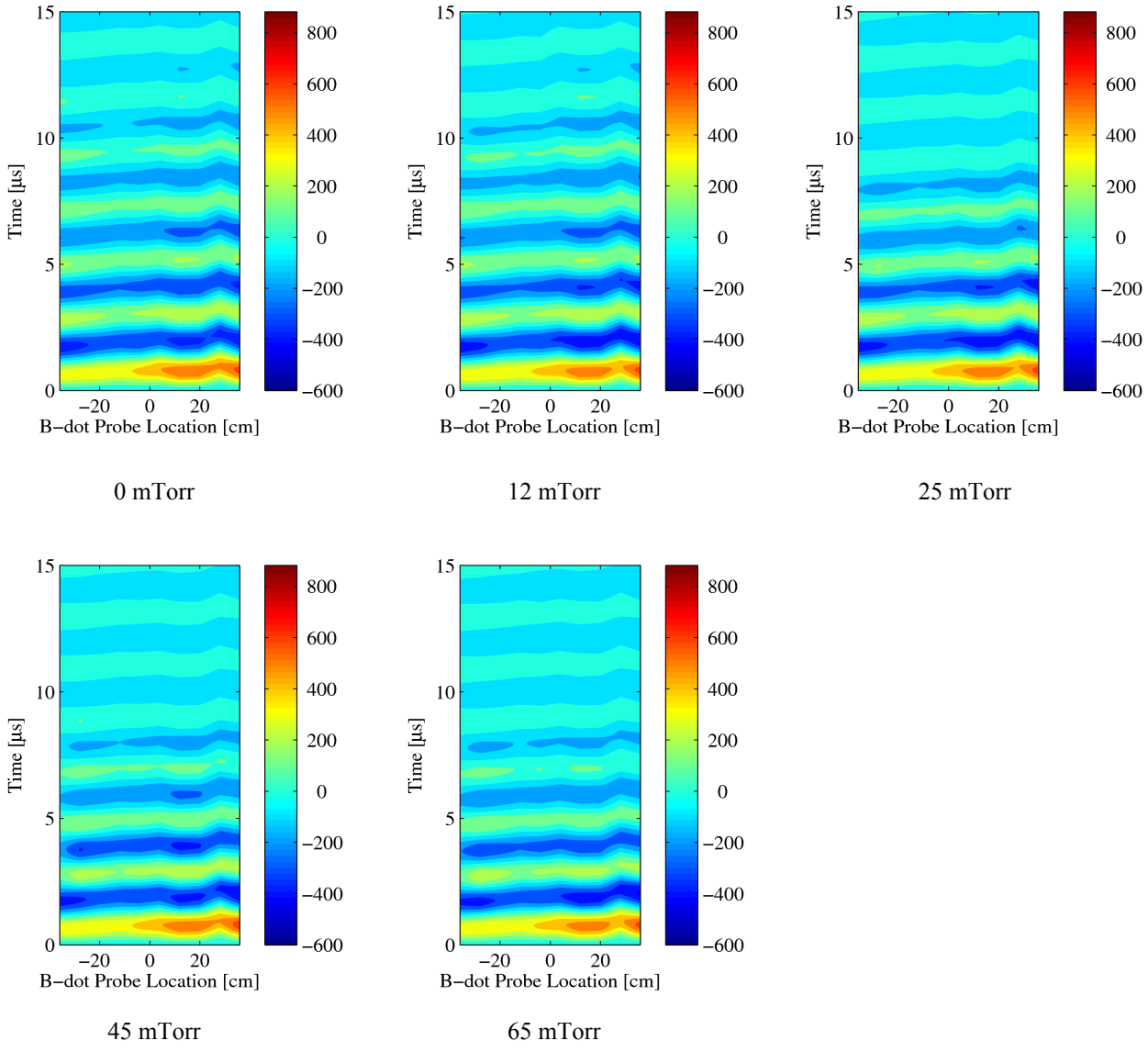

Figure 19: B-dot probe array data for air at 15 kV as a function of probe location, time, and pressure measured in G

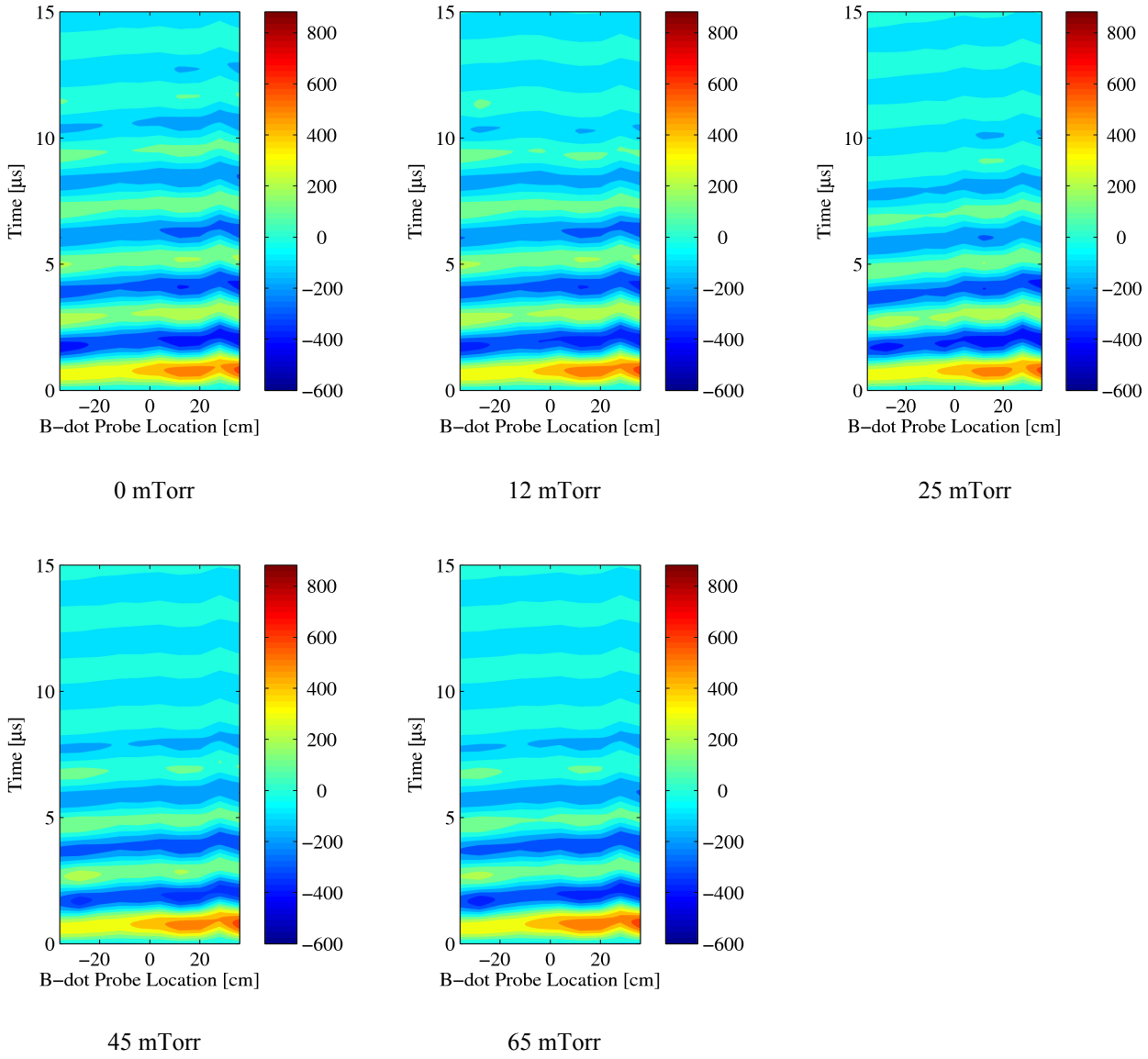

Figure 20: B-dot probe array data in argon at 15 kV as a function of probe location, time, and pressure measured in G

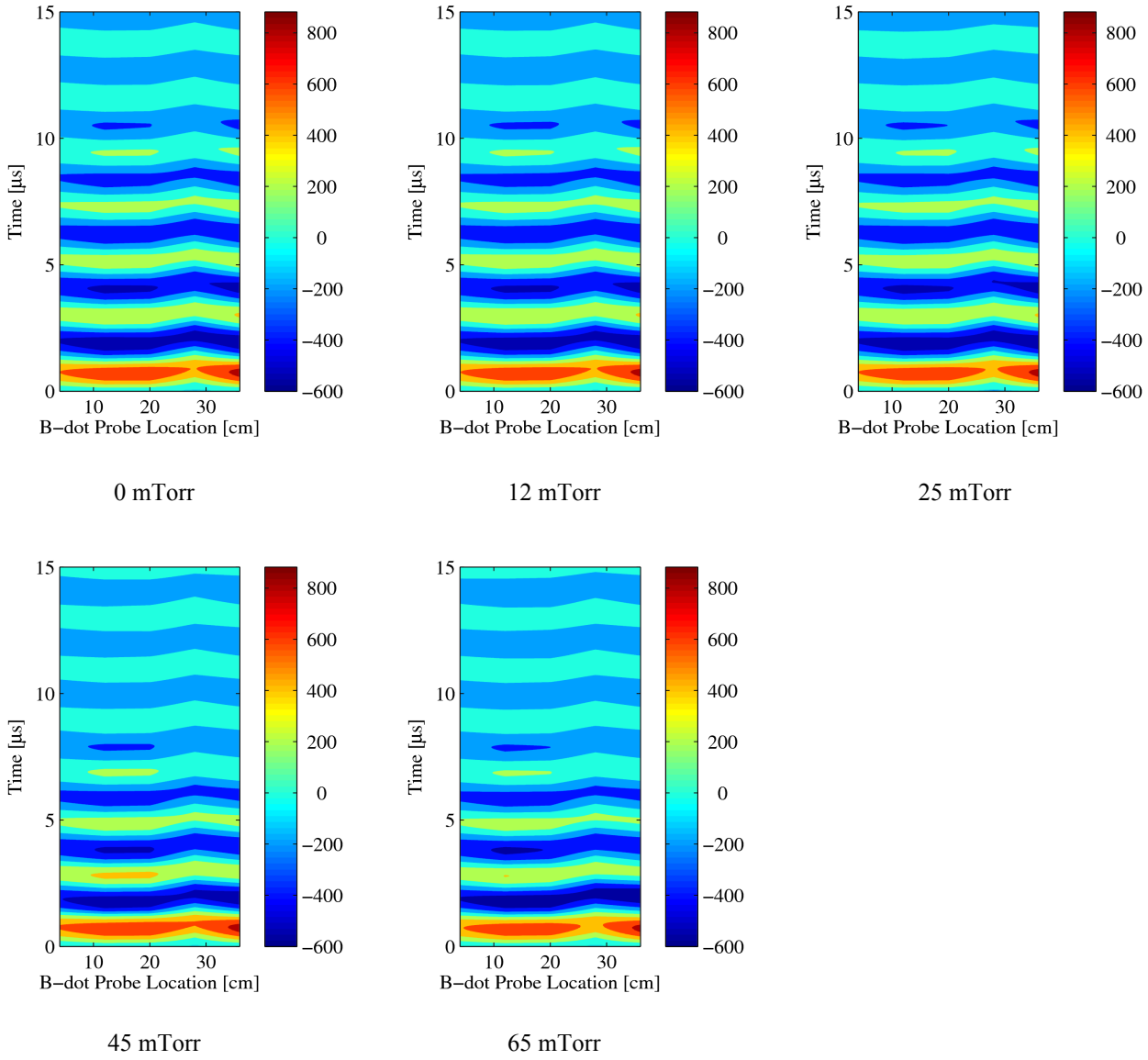

Figure 21: B-dot probe array data in air at 20 kV as a function of probe location, time, and pressure measured in G

All 15 plots indicate that probe ten records the largest magnetic field. This result is expected if current is indeed pooling at the end of the coil as the EMC Studio simulation would suggest. Of concern, however, is that this same trend is not observed at the other coil edge. Probe one is consistently the probe with the lowest measured magnetic field. Additionally, if all probes are in phase with each other, all the horizontal contour lines seen after ten µs should be parallel. Instead, a ripple is noticed at probe nine's location. This is the same results observed in Figure 10. B-dot probe nine is proceeds the waveforms of the nine other probes by almost 90º. The larger measured field strength and phase is likely more a result of experimental setup than errors in the probes themselves. Probe ten is the closest to the vacuum facility and probe nine is second closest. The transmission lines of the various probes move away from probes nine and ten towards probe one. This provides a few possible explanations for the observed trends. One possibility is that the vacuum facility, being one large conductor, is interfering with the magnetic field of the coil resulting in the possible phase change. As the probes move away from the chamber the amount of ripple observed in the contour plots decreases. Another consideration is the location of the transmission lines relative to the various probes. Probe ten is constructed with the longest segment of SMA coaxial cable. While this cable is shielded, being

run directly under the theta coil is likely to disturb measurements. If the SMA cable does not shield the probe output from this electromagnetic noise, the SMA cable will act like an radio antenna. The larger the antenna, the more signal picked up. This would account for the decreasing probe magnitude from right to left in the above contour plots. Another trend that is observed is that as pressure increases, the duration of the discharge decreases. At lower pressures, plasma formation is more sporadic. Plasma is observed in tests done in pressures as low as two mTorr. But this configuration failed to produce plasma from four mTorr to 20 mTorr. But in the cases when this does occur, all tests show that probes six through ten are more likely measure plasma formation at these lower pressures. The exception is the 15 kV discharge in air at a fill pressure of 55 mTorr. This is the only test that probes six through ten failed to see plasma when probes one through five do. Because probes not used during a test are left disconnected, this may indicate that the discharge characteristics of MPX are coupled to the diagnostics or their support hardware. These effects are to be the study of a forthcoming paper.

At zero mTorr, oscillation is observed out to 25 μs versus 17 μs at 65 mTorr. For the same discharge level with argon, this increase in signal decay occurs sooner for a given pressure than error. Argon also sees a total discharge time of 25 μs at zero mTorr, but decreases to 21 μs at 12 mTorr. The shortest total discharge time of argon at 15 kV is 18 μs at occurs pressures as low as 25 mTorr. This indicates that consistent, repeatable plasma formation in argon is achieved for pressures between 25 and 65 mTorr. The 20 kV discharge with air has the longest decay time. This is a result of increased energy with a fixed energy dissipation rate. As observed with the 15 kV discharge with air, consistent formation is not evident at pressures lower than 45 mTorr.

The maximum magnetic fields recorded for the 15 kV discharges in air, the 15 kV discharges in argon, and the 20 kV discharges in air are 675 G, 695 G, and 882 G. This represents an associate error 41.9%, 51.2%, and 41.2%, respectfully, from the predicted values of EMC Studio. At 15 kV, the maximum magnetic fields recorded by B-dot probes five and six, the ones used in calibration, are 457 G and 504 G, respectfully, and 614 G for probe six at 20 KV. This corresponds to a maximum error of 0.53%, 9.65%, and 1.50%, respectfully. This indicates that the calibration values used for the B-dot probes remained relatively unchanged throughout testing with probe six at 15 kV being higher than desired.

2 Flux loops

Data acquired using the flux loop array is discussed in this section. Figure 22 is a contour plot of the magnetic field recorded by all ten flux loops for a 15 kV discharge as a function of probe location and time. Similarly, Figure 23 presents the same data but with argon as the fill gas. Figure 24 plots a 20 kV discharge in air. As with the B-dot data, Figure 24 consists of data collected from only five probes (probes six through ten).

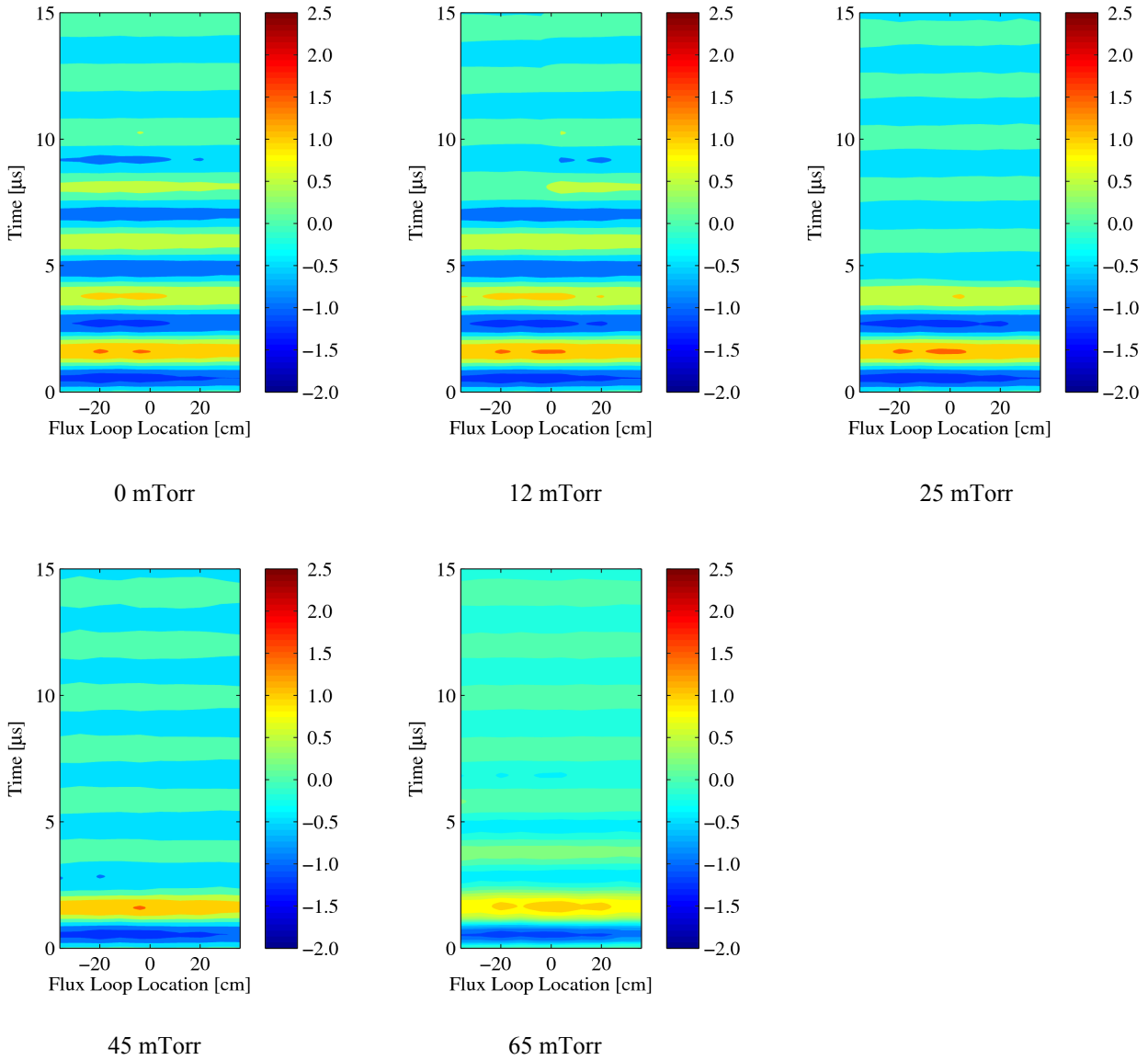

Figure 22: Flux loop array data in air at 15 kV as a function of probe location, time, and pressure measured in mWb

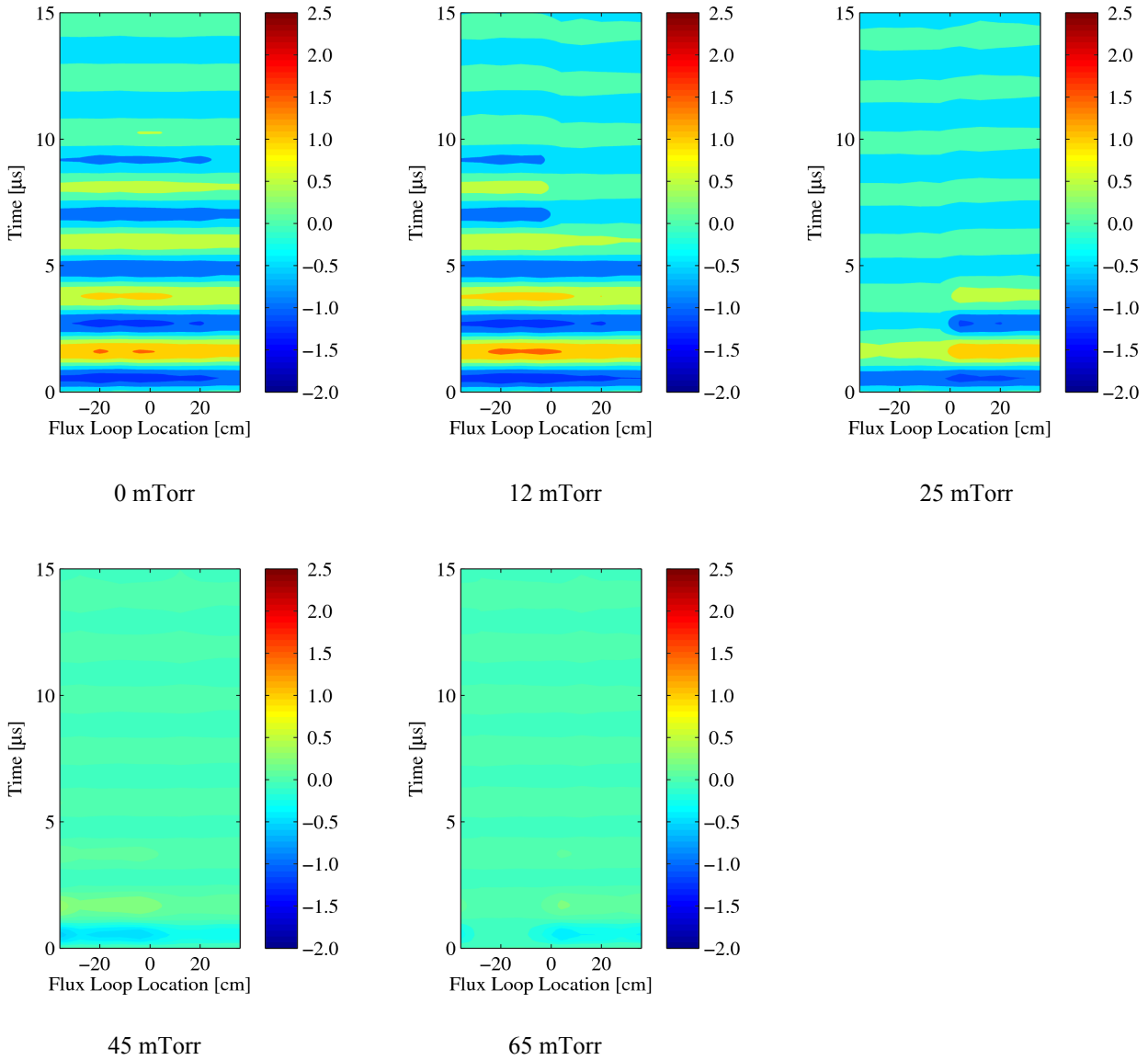

Figure 23: Flux loop array data in argon at 15 kV as a function of probe location, time, and pressure measured in mWb

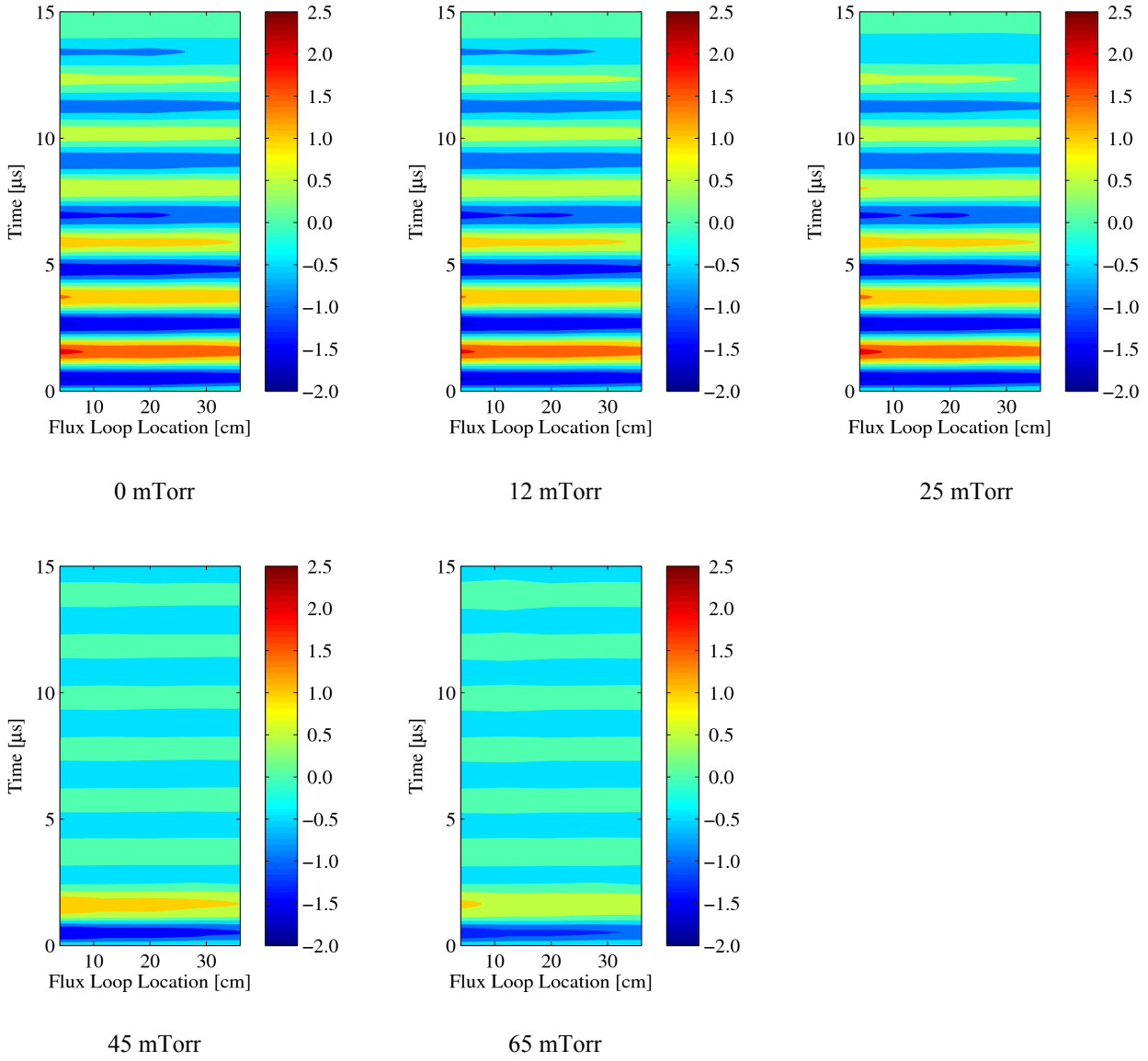

Figure 24: Flux loop array data in air at 20 kV as a function of probe location, time, and pressure measured in mWb

Unlike the contour lines observed in the B-dot probe results, the flux loops maintain relatively parallel contour lines during discharge. Maximum magnetic flux in nearly every test is observed at probes five and six with probe three contributing slightly less frequently. The trend that the discharge duration decreases with increasing pressures is identical to what is seen in the B-dot data. The most significant difference observed between the flux loop output and B-dot probe output is how quickly the magnetic flux decreases with time. As pressure increases, the output of the flux loops decreases rapidly compared to the relatively constant B-dot discharges. In the 15 kV discharge with air at a pressure of zero mTorr, significant flux is measured for nearly nine μs. However, at 25 mTorr the duration of the flux output is nearly completed at four μs. At 65 mTorr, only one period of flux data is observed before it decays to zero. This trend is more pronounced 15 kV discharges with argon. The same results are seen at zero mTorr, but at a pressure of 45 mTorr, the flux data doesn't even complete one full period before decaying to zero. This is because the time for the 45 mTorr case to deviate from the zero mTorr case is only 0.7 μs. If this deviation is a result of plasma or occurs near the time of plasma formation, these results make sense. As soon as plasma is

generated, the magnetic flux is immediately absorbed into the plasma. Indeed, the results from 65 mTorr in argon seemingly show that no discharge occurred even though plasma presence is observed visually with the FASTCAM high speed camera.

Maximum magnetic flux of 1.62 mWb, 1.59 mWb, and 2.17 mWb are observed for the 15 kV discharges in air and argon and the 20 kV discharge in air, respectfully. Using the ideal magnetic field provided by EMC Studio to calculate the theoretical magnetic flux at the center of the coil, these values correspond to errors of 41.8%, 28.9%, and 40.1%, respectfully.

E. Energy Deposition into Plasma

This section investigates the amount of energy absorbed by the plasma as functions of time and pressure for discharges at 15 and 20 kV in air and 15 kV in argon. Figure 25 shows the total energy absorbed by the plasma at a specific time during the discharge as a function of fill pressure. Energy absorption contours are presented for the 15 kV discharges in air and argon and 20 kV discharges in air.

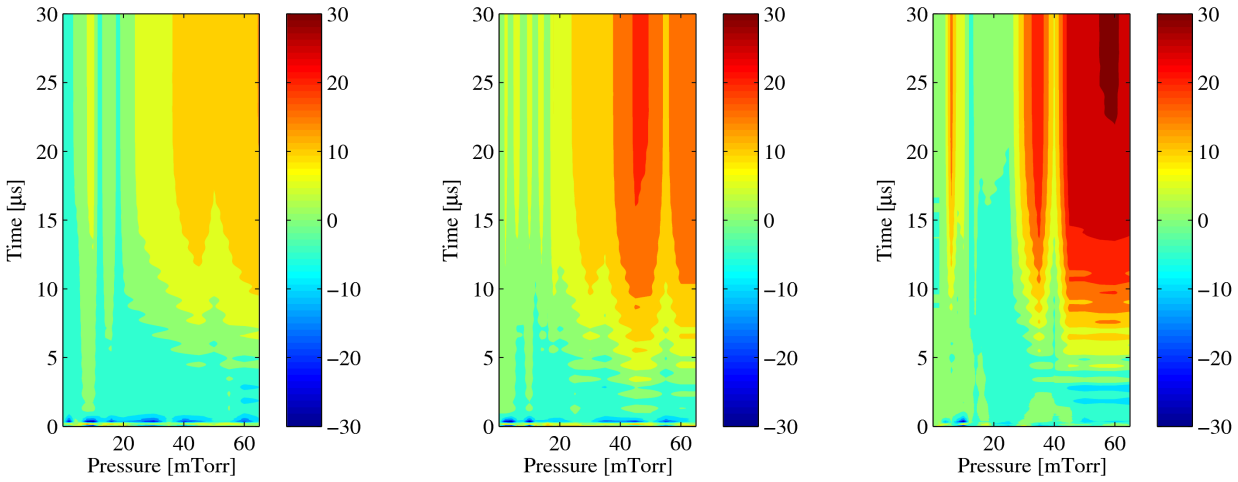

Figure 25: Energy deposited into plasma for various combinations of gas species and voltage as functions of pressure and time measured in J

The data in Fig. 25 are found by first looking at the magnetic energy stored within the theta coil. At any given moment, the magnetic energy stored in an inductor is proportional to square of the instantaneous current flowing through the coil. Since the current of the discharge is known, the magnetic energy as a function of time can be calculated. By comparing the magnetic energy at any given time for a test to the zero mTorr case, the total amount of magnetic energy lost from the system can be calculated. The only difference from a zero mTorr case and any other case is the presence of a fill gas. Therefore, two assumptions are made: one, that 100% of the energy deficit between tests is absorbed by the plasma. Two, 100% of the capacitive energy is converted to magnetic energy (i.e., no losses). By multiplying the fraction of magnetic energy absorbed by the total energy stored in the capacitor at the beginning of the test, the amount of electrical energy absorbed into the plasma is determined.

As pressure increases from zero, the required magnetic energy needed to break down the gas decreases according to the passion curve.[20] This trend is observed in Fig. 25. More energy is deposited into the plasma because less energy is wasted during plasma formation. If more tests were conducted at higher pressures, it is likely that the trend would reverse and less energy would be absorbed by the plasma. The tests using argon at 15 kV and air at 20 kV show what is likely the start of this tend. Plasma energy absorption into argon maximized at 45 mTorr with a maximum of 20.6 J being absorbed by the plasma. After 45 mTorr, the amount of energy deposited into the plasma starts to decrease. In the case of air discharges at 20 kV, more energy is stored in the capacitor initially. So even if the same fraction of energy is deposited, the total amount of energy is greater. The largest amount of energy absorbed is 30.3 J and occurs at a pressure of 60 mTorr during a 20 kV discharge in air. This is 21.4% of the stored

electrical energy. Only one pressure case exists after this point. While the data indicates that a peak energy transfer efficiency at 60 mTorr, insufficient data are present to state this conclusively.

F. Deviation Times

This section presents the deviation of probe signals as a function of location. Only a partial set of values is presented to convey the general trends found in the data. The left-hand plot in Figure 26 is the deviation times associated with the flux loops during 15 kV discharges in air. The right-hand plot presents the results of 15 kV testing with argon.

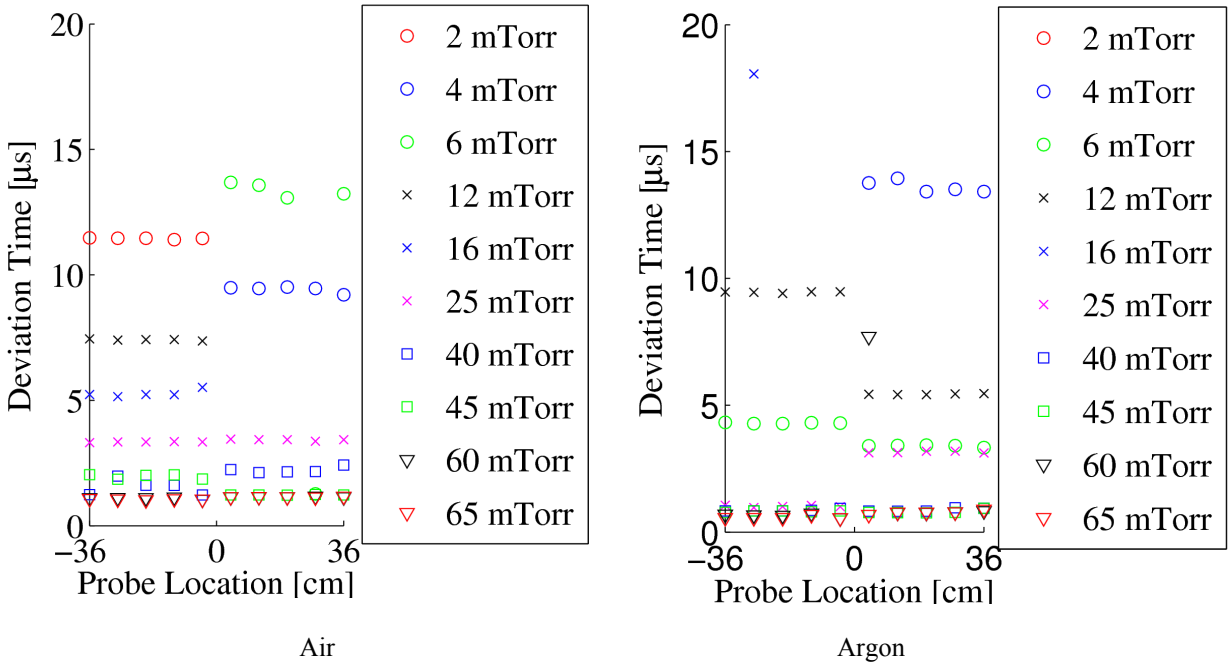

Figure 26: Times at which waveform deviates from the zero mTorr waveform

As observed in the contour plots presented previously (sec. IV.D.), argon reaches a state of high repeatability at lower fill pressures. Discharges in air do not stabilize around specific time until fill pressures of 60 mTorr or more. Argon reaches a repeatable state at 40 mTorr. Additionally, The stabilized deviation times for air and argon are 1.1 µs and 0.77 µs, respectfully. This correlates with previous data that show magnetic flux attenuating far sooner than the magnetic field when the system is filled with argon rather than air. Additionally, the ideal pressure for energy deposition into an argon plasma occurred at a fill pressure of 45 mTorr which falls into the region of stability for 15 kV discharges of MPX.

G. High Speed Camera

Figure 27 show the evolution of plasma withing the quartz vessel at several pressures. The lower pressures were not considered because of their lower reliability to form plasma consistently. Time is presented along the top of the figure and is measured from some unknown trigger time, t_0. The time between frames is known, and is approximately 9.13 µs. For some pressures, plasma persists for four frames after initial creation. Additionally, three tests show plasma formation a frame sooner than the other 23 tests. Therefore, a total of six frames have been included for comparison for each pressure. These frames are placed sequentially from left to right showing the time evolution of the plasma. The vertical axis of Figure 27 is the fill pressure in mTorr of air during the test.

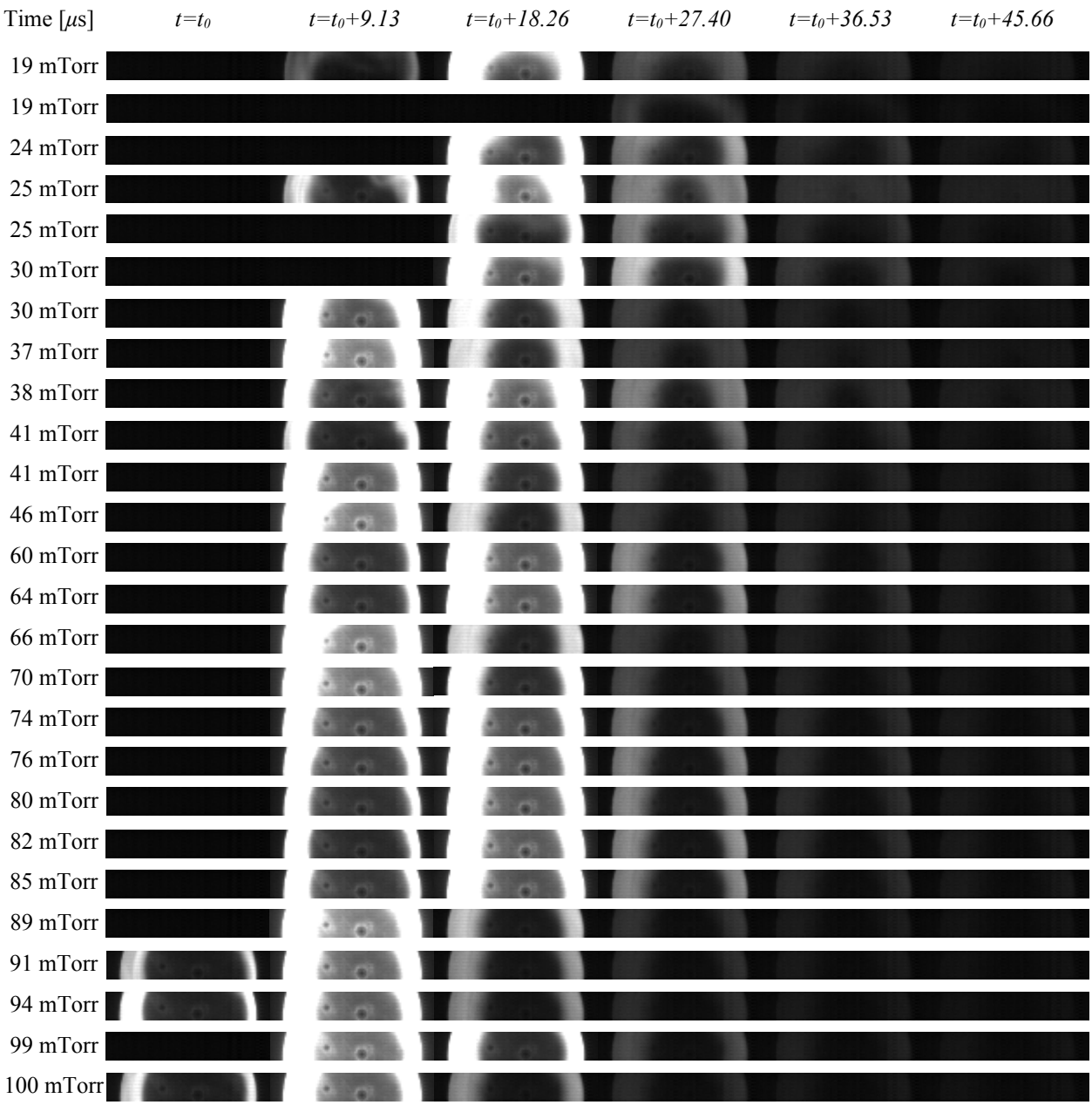

Figure 27: Plasma discharges recored with FASTCAM-1024PCI high speed camera

A few pressures are included twice (19, 25, 30, and 41 mTorr) due to the inconsistencies of discharges noted at lower pressures. For example, the first two tests occur use a fill pressure of 19 mTorr. The first pressure shows has four frames where plasma is observed. The second test, while at the same pressure, barely records one frame. Because the frame rate of the camera is long compared to the discharge frequency (5:1), portions of the plasma formation process will be missed. However, it is unlikely that the absence of plasma is seen in the second test is due to camera timing. Far more likely is that a lower energy plasma is formed. As pressure is increased past 30 mTorr, the output of the high speed camera is almost identical up to 91 mTorr. At 91 mTorr, plasma is observed one frame (~9.13 μs) sooner than previous cases. The first frame in this discharge shows a thinner ring of plasma than is observed in the second frame of the previous tests. The second frame of the 91 mTorr test shows an increased

plasma thickness. Without knowing the various triggering times of these test, any meaningful correlation beyond the qualitative can be made.

V. Conclusions

This paper presents the on-going efforts to characterize the discharge characteristics and pre-ionization properties in the FRC test article, MPX. Test are conducted using air during 15 and 20 kV discharges and argon at 15 kV at pressures ranging from zero mTorr to 65 mTorr and their data presented. Commercially available off-the-self surface mount inductors are used for magnetic field (B-dot) probes. These probes come with a calibration factor from the manufacture which is verified through simulations using EMC Studio. A calibration value of 108.8 turns-mm^2 is used for the B-dot probes.

Custom voltage dividers are constructed to attenuate the high voltage output signal from the flux loops. A calculated attenuation of 1:154 agrees well with the average measured attenuation of 153.9:1. The magnetic flux probes (flux loops) are calibrated using the values given by the calibrated B-dot probes. A calibration factor of 0.6758 Wb/(V-s) is applied to the integrated flux loop data to determine the magnetic flux associated with the discharge.

Methods of post processing the data are discussed. Specifically, the issue of physical integrators versus numerical post-processing is discussed. The method for post-processing the data is discussed at length in section IV.C. Results of testing are plotted in contour plots for convenience. The data indicate that argon plasma is formed at lower pressures than air and has a region of increased repeatability from 40 mTorr to 65 mTorr while air is limited to the smaller range of 60-65 mTorr. Argon plasma achieves maximum energy absorption at 45 mTorr during a 15 kV discharge, absorbing just over 20 J (25.1%) of energy from the system.

Finally, qualitative observation of the plasma formation process using a FASTCAM 1024PCI high speed camera. Plasma repeatability is confirmed for pressures of air greater than 41 mTorr for 15 kV discharges.

Acknowledgements

The authors of this paper would like to thank the Air Force Office of Scientific Research (grant FA9550-10-1-0204, grant monitor Dr. Mitat Birkan) for funding this research.

References

1 Bellan P.M., *Spheromaks: A Practical Application of Magnetohydrodynamic Dynamos and Plasma Self-Organization*, Imperial College Press, London, 2000.

2 Brown D.L., Beal B.E. & Haas J.M., "Air Force Research Laboratory High Power Electric Propulsion Technology Development," (2009).

3 Martin A. & Eskridge R., "Electrical Coupling Efficiency of Inductive Plasma Accelerators," *Journal of Physics D: Applied Physics*, Vol. 38, Nov, 2005, pp. 4168-4179.

4 Ruden E.L., Sanchez P.G., Taccetti J.M., Tuszewski M., Waganaar W.J., et al., "A High Density Field Reversed Configuration Plasma for Magnetized Target Fusion," Nov, 2003.

5 Niemela C.S. & Kirtley D.E., *Initial Results on an Annular Field Reversed Configuration Plasma Translation Experiment*, Edwards AFB, CA, 2008.

6 Slough J.T. & Votroubek G., "Magnetically Accelerated Plasmoid (MAP) Propulsion," *42nd AIAA Joint Propulsion Conference*, Sacramento, CA, July 9-12, 2006.

7 Slough J.T., "Propagating Magnetic Wave Plasma Accelerator (PMWAC) for Deep Space Exploration," (1999).

8 Slough J.T., "Earth to Orbit based on a Reciprocating Plasma Liner Compression of Fusion Plasmoids," *43rd AIAA Joint Propulsion Conference & Exhibit*, Cincinnati, OH, July 8 - 11, 2007.

9 Kirtley D.E., Brown B., Gallimore A. & Haas J., "Details on an AFRL Field Reversed Configuration Plasma Device," *29th International Electric Propulsion Conference*, Princeton, NJ, Oct. 31 - Nov. 4, 2005.

10 Kirtley D.E., “Study of the Synchronous Operation of an Annular Field Reversed Configuration Plasma Device”. Department of Aerospace Engineering, University of Michigan. 2008.

11 Kirtley D.E., Gallimore A., Haas J. & Reilly M., "High Density Magnetized Toroid Formation and Translation within XOCOT: An Annular Field Reversed Configuration Plasma Concept," *30th International Electric Propulsion Conference*, Florence, Italy, Sept. 17-20, 2007.

12 Koelfgen S.J., Eskridge R., Lee M.H., Martin A., Hawk C.C., et al., "Magnetic and Langmuir Probe Measurements on the Plasmoid Thruster Experiment (PTX)," *40th Joint Propulsion Conference*, Fort Lauderdale, FL., July 11-14, 2004.

13 Koelfgen S.J., Hawk C.W., Eskridge R., Lee M.H., Martin A., et al., "A Plasmoid Thruster for Space Propulsion," *39th AIAA Joint Propulsion Conference*, Huntsville, AL, July 20-23, 2003.

14 Slough J.T., Kirtley D. & Weber T., "Pulsed Plasmoid Propulsion: The ELF Thruster," *31th International Electric Propulsion Conference*, Ann Arbor, MI, Sept. 20-24, 2009.

15 Kirtley D., Slough J., Pihl C., Meier E. & Milroy R., "Pulsed Plasmoid Propulsion: Air-Breathing Electromagnetic Propulsion," *32nd International Electric Propulsion Conference*, Kurhaus, Wiesladen, Germany, Sept. 11-15, 2011.

16 Fimognari P.J., Cassibry J.T. & Ims K., "Effects of Pre-ionization and Bias Field on Plasmoid Formation and Acceleration," *43rd AIAA Joint Propulsion Conference*, Cincinnati, OH, July 8-11, 2007.

17 Niemela C.S. & King L.B., "Numerical Optimization of an Annular Field Reversed Configuration Translation Experiment," *31st International Electric Propulsion Conference*, Ann Arbor, MI, Sept. 20-24, 2009.

18 Tuszewski M., "Field Reversed Configurations," *Nuclear Fusion*, Vol. 28, No. 11, 1988, pp. 2033-2092.

19 Rej D.J. & Tuszewski M., "A Zero-Dimensional Transport Model for Field-Reversed Configurations," *American Institute of Physics: Physics Fluids*, Vol. 27, Jun, 1984, pp. 1514-1520.

20 Burm K., "Breakdown Magnetic Field in an Inductively Coupled Plasma," *Physics Letters A*, (2008), **372,** pp. 6280-6283.

21 Um E.. “Diamagnetic Loop Diagnostic System for the TRAP Experiment”. University of Washington. 1994.

22 Taccetti J.M., Intrator T.P., Wurden G.A., Zhang S.Y., Aragonex R., et al., "FRX-L: A Field-Reversed Configuration Plasma Injector for Magnetized Target Fusion," *Review of Scientific Instruments*, Vol. 74, No. 10, Oct, 2003, pp. 4314-4323.

23 Pahl R.A., Meeks W.C. & Rovey J.L., "Pre-Ionization Plasma in an FRC Test Article," *47th Joint Propulsion Conference*, San Diego, CA, July 31 - Aug. 3, 2011.

24 Lucien F., "Bdot Plasma Probe," 2008.

25 Smith H.G., *Construction and Calibration of a Tri-Directional Magnetic Probe for the VASIMR Experiment on mini-RFTF*.

26 Zhang S.Y., Tejero E.M., Taccetti J.M., Wurden G.A., Intrator T.P., et al., "Separatrix Radius Measurement of Field-Reversed Configuration Plasma in FRX-L," *Review of Scientific Instruments*, Vol. 75, No. 10, 2004, pp. 4289-4292.

27 Cross R.C. & Collins G.A., "Compensated RC Integrators," *American Journal of Physics*, Vol. 49, No. 5, May, 1981, pp. 479-480.